

# Simultaneous measurement of the photodisintegration of ${}^4\text{He}$ in the giant dipole resonance region

T. Shima,<sup>\*</sup> S. Naito,<sup>†</sup> and Y. Nagai

*Research Center for Nuclear Physics, Osaka University, Ibaraki, Osaka 567-0047, Japan*

T. Baba,<sup>‡</sup> K. Tamura,<sup>§</sup> and T. Takahashi<sup>¶</sup>

*Department of Physics, Tokyo Institute of Technology, Meguro, Tokyo 152-8551, Japan*

T. Kii and H. Ohgaki

*Institute of Advanced Energy, Kyoto University, Uji, Kyoto 611-0011, Japan*

H. Toyokawa

*Photonics Research Institute, National Institute of Advanced Industrial Science and Technology, Tsukuba, Ibaraki 305-8568, Japan*

(Dated: July 4, 2018)

We have performed for the first time the simultaneous measurement of the two-body and three-body photodisintegration cross-sections of  ${}^4\text{He}$  in the energy range from 21.8 to 29.8 MeV using monoenergetic pulsed photons and a  $4\pi$  time projection chamber containing  ${}^4\text{He}$  gas as an active target in an event-by-event mode. The photon beam was produced via the Compton backscattering of laser photons with high-energy electrons. The  ${}^4\text{He}(\gamma, p){}^3\text{H}$  and  ${}^4\text{He}(\gamma, n){}^3\text{He}$  cross sections were found to increase monotonically with energy up to 29.8 MeV, in contrast to the result of a recent theoretical calculation based on the Lorentz integral transform method which predicted a pronounced peak at around 26–27 MeV. The energy dependence of the obtained  ${}^4\text{He}(\gamma, n){}^3\text{He}$  cross section up to 26.5 MeV is marginally consistent with a Faddeev-type calculation predicting a flat pattern of the excitation function. The cross-section ratio of  ${}^4\text{He}(\gamma, p){}^3\text{H}$  to  ${}^4\text{He}(\gamma, n){}^3\text{He}$  is found to be consistent with the expected value for charge symmetry of the strong interaction within the experimental uncertainty in the measured energy range. The present results for the total and two-body cross-sections of the photodisintegration of  ${}^4\text{He}$  are compared to previous experimental data and recent theoretical calculations.

PACS numbers: 21.45.+v; 21.30.Fe, 24.30.Cz, 25.10.+s, 25.20.-x; 26.30.+k

## I. INTRODUCTION

The unique feature of  ${}^4\text{He}$  as the lightest self-conjugate nucleus with the simplest closed-shell structure prompts both experimentalists and theorists to study its photodisintegration reaction in the giant dipole resonance (GDR) region. Since the reaction proceeds mainly by an electric dipole (E1) transition in the GDR region, the photodisintegration study provides a wealth of fundamental information on nucleon-nucleon (NN) interactions, meson exchange currents [1] as well as the possibility to study the charge symmetry of the strong interaction [2]. The photodisintegration study also gives important insight on the rapid neutron capture process (r-process) nucleosyn-

thesis induced by neutrino-driven wind from a nascent neutron star [3], since the neutrino transitions are the direct analogs of the giant electric dipole resonance observed in the photodisintegration [3, 4].

A considerable amount of theoretical work on the photodisintegration of  ${}^4\text{He}$  has been carried out in the GDR region. Above 50 MeV, the two-body  ${}^4\text{He}(\gamma, p){}^3\text{H}$  and  ${}^4\text{He}(\gamma, n){}^3\text{He}$  cross sections as well as the total cross section are well described by a plane-wave approximation, in which final state interactions (FSI) are known to play a minor role [5]. Below 30 MeV, however, these cross sections are sensitive to FSI, meson exchange currents as well as to the choice of NN interaction [5, 6]. Recently two different methods, one based on the Lorentz integral transform (LIT) [7, 8] and another based on Faddeev-type Alt-Grassberger-Sandhas (AGS) integral equations [9], have been developed to accurately describe the low-energy dynamics of the  ${}^4\text{He}$  photodisintegration. Here it should be mentioned that although these models are quite different from each other, the calculated photodisintegration cross sections of  ${}^3\text{H}$  and  ${}^3\text{He}$  provided by these models agree with each other with high precision for the same NN interaction and three-nucleon forces (3NF) [10]. However, the values of the photodisintegration cross section of  ${}^4\text{He}$  calculated by the same models differ significantly from each other. According to the calculation

---

<sup>\*</sup>Electronic address: shima@rcnp.osaka-u.ac.jp

<sup>†</sup>Present address: Toshiba Co., Ltd., 8, Shinsugita-Cho, Isogo, Yokohama 235-8523, Japan

<sup>‡</sup>Present address: Hitachi, Ltd., 1-280, Higashi-koigakubo, Kokubunji, Tokyo 185-8601, Japan

<sup>§</sup>Present address: ERNST&YOUNG SHINNIHON, Hibiya Kokusai Bldg., 2-2-3, Uchisaiwai-cho, Chiyoda-ku, Tokyo 100-0011, Japan

<sup>¶</sup>Present address: Ricoh Co., Ltd., 30-1, Saho, Yashiro-cho, Katogun, Hyogo 673-1447, Japan

performed with the LIT method, both the total and two-body cross sections show a pronounced GDR peak at around 26–27 MeV, and the total cross section fully satisfies both the E1 sum rule and the inverse-energy-weighted E1 sum rule [7, 8]. On the other hand, the calculation based on the AGS method, carried out for the  ${}^4\text{He}(\gamma, n){}^3\text{He}$  cross section, shows a flat pattern below the three-body threshold energy of 26.1 MeV, and the calculated cross section at 26.1 MeV is only about 60% of the value derived by the LIT method [9].

Experimentally the two-body, three-body, and total photodisintegration cross sections of  ${}^4\text{He}$  have been measured in the energy range from 20 to 215 MeV using quasi-monoenergetic photon beams and/or bremsstrahlung photon beams. Concerning the two-body  ${}^4\text{He}(\gamma, p){}^3\text{H}$  and  ${}^4\text{He}(\gamma, n){}^3\text{He}$  reactions, their inverse, the nucleon capture reactions, were used to derive the photodisintegration cross sections. Previous data for the two-body and total cross sections are shown in Figs. 1(a), 1(b), and 1(c), respectively. It is quite interesting to note that above 35–40 MeV most of the previous  ${}^4\text{He}(\gamma, p){}^3\text{H}$  and  ${}^4\text{He}(\gamma, n){}^3\text{He}$  data agree with each other within their respective data sets [9]. However, there appear to be discrepancies especially in the peak region of 25–26 MeV, where the data show either a pronounced GDR peak or a fairly flat excitation function as shown in Figs. 1(a) and 1(b). The experimental methods and their results in the previous measurements are briefly described below to obtain some hints of the origin of the large discrepancies mentioned above. Here, it would be quite interesting to note the discrepancies related to different photon probes. The  ${}^4\text{He}(\gamma, p){}^3\text{H}$  cross section,  $\sigma(\gamma, p)$ , was measured by detecting the protons by means of a NE213 liquid scintillator [11] and/or a Si(Li) detector array [12]. Note that the latest result by Hoorebeke *et al.* using 34 MeV end-point bremsstrahlung photons [12] is larger than the data by Bernabei *et al.* [11] using a monochromatic photon beam by about 40% at around 30 MeV. The difference of these two data sets, however, becomes smaller with increasing the  $\gamma$ -ray energy, and they agree with each other at 33 MeV within the experimental uncertainty. The  ${}^3\text{H}(p, \gamma){}^4\text{He}$  reaction cross section was measured using a tritium target absorbed into various metals by detecting a  $\gamma$ -ray by means of a NaI(Tl) detector [13–19]. Note that the latest result by Hahn *et al.* [19] is about 20% larger than that by Feldman *et al.* [18]. In summary, the  ${}^4\text{He}(\gamma, p){}^3\text{H}$  cross section derived from both the photodisintegration and the inverse reaction shows a large discrepancy between different data sets, and the difference is quite large (about 50%) at  $E_\gamma = 25$  MeV.

On the other hand, the  ${}^4\text{He}(\gamma, n){}^3\text{He}$  cross section,  $\sigma(\gamma, n)$ , was measured by detecting the neutrons with  $\text{BF}_3$  neutron detectors and using bremsstrahlung photons [20, 21] and/or monoenergetic photons [22]. The results obtained using bremsstrahlung photons are larger by about 30~100% than the result obtained using monoenergetic photons in the region between 25 and 30 MeV. Similarly to the case noted above, the difference

between these data sets with different photon beams becomes smaller with increasing  $\gamma$ -ray energies, and they agree with each other at 35 MeV within an experimental uncertainty. The  ${}^3\text{He}(n, \gamma){}^4\text{He}$  reaction cross section was measured by detecting  $\gamma$ -rays with a NaI(Tl) and/or a BGO detector [23, 24], and their measured cross sections in the  $\gamma$ -ray energy range from 22 to 33 MeV agree with the  ${}^4\text{He}(\gamma, n){}^3\text{He}$  data by Berman *et al.* within the experimental uncertainty [22].

Simultaneous measurements of the cross-sections for all reaction channels were performed by detecting charged fragments from the photodisintegration by means of cloud chambers using bremsstrahlung photon beams in the energy range from 21.5 to 215 MeV [25, 26], from 20.5 to 150 MeV [27, 28], and from 24 to 46 MeV [29, 30], respectively. The results obtained with these measurements are 30~70% larger than the cross sections obtained with monoenergetic photon beams or tagged photon beams.

The elastic photon scattering of  ${}^4\text{He}$  was performed in the energy range from 23 to 34 MeV to derive indirectly the total photodisintegration cross section of  ${}^4\text{He}$  [31]. The results by Gorbunov *et al.* [26] agree with those by Arkatov *et al.* [27] and also by Wells *et al.* [31] within the experimental uncertainty (see Fig. 1(c)).

The electromagnetic property of the photodisintegration cross-section of  ${}^4\text{He}$  in the giant resonance region has been discussed in terms of the electric dipole (E1) radiation [9]. Experimentally below 26.6 MeV the E1 dominance with a small M1 contribution of less than 2% has been shown by measuring angular distributions of cross-sections and/or analyzing powers for the inverse  ${}^3\text{H}(p, \gamma){}^4\text{He}$  reaction [16, 17, 32]. Theoretically an E2 contribution to the total two-body cross-section is estimated to be small, about 6%, even at  $E_\gamma = 60$  MeV [9].

The cross-section ratio of  ${}^4\text{He}(\gamma, p){}^3\text{H}$  to  ${}^4\text{He}(\gamma, n){}^3\text{He}$ ,  $R_\gamma = \sigma(\gamma, p)/\sigma(\gamma, n)$ , in the GDR region has been used to test the validity of the charge symmetry of the strong interaction. When charge symmetry is valid, the ratio is about unity for pure E1 excitations [2].  $R_\gamma$  has been obtained experimentally with values ranging from 1.1 to 1.7 by separate measurements of  $\sigma(\gamma, p)$  and  $\sigma(\gamma, n)$  in the GDR region [17]. From simultaneous measurements of the  ${}^4\text{He}(\gamma, p){}^3\text{H}$  and  ${}^4\text{He}(\gamma, n){}^3\text{He}$  reactions using cloud chambers and bremsstrahlung photon beams,  $R_\gamma$  was obtained as 1.0~1.5 in the energy range from 23 to 44 MeV [25, 27, 29]. Recently  $R_\gamma$  of 1.1 was obtained by a simultaneous ratio measurement of the  ${}^4\text{He}(\gamma, p){}^3\text{H}$  and  ${}^4\text{He}(\gamma, n){}^3\text{He}$  reactions in the energy range from 25 to 60 MeV [33]. The measurement was performed by detecting a charged fragment emitted at  $90^\circ$  with respect to an incident tagged photon beam direction by means of windowless  $\Delta E$ -E telescopes. Here an angular distribution effect of a fragment was corrected for using theory.

In summary, although considerable experimental efforts have been made in determining  $R_\gamma$ , there remains a large discrepancy between separate measurements and si-

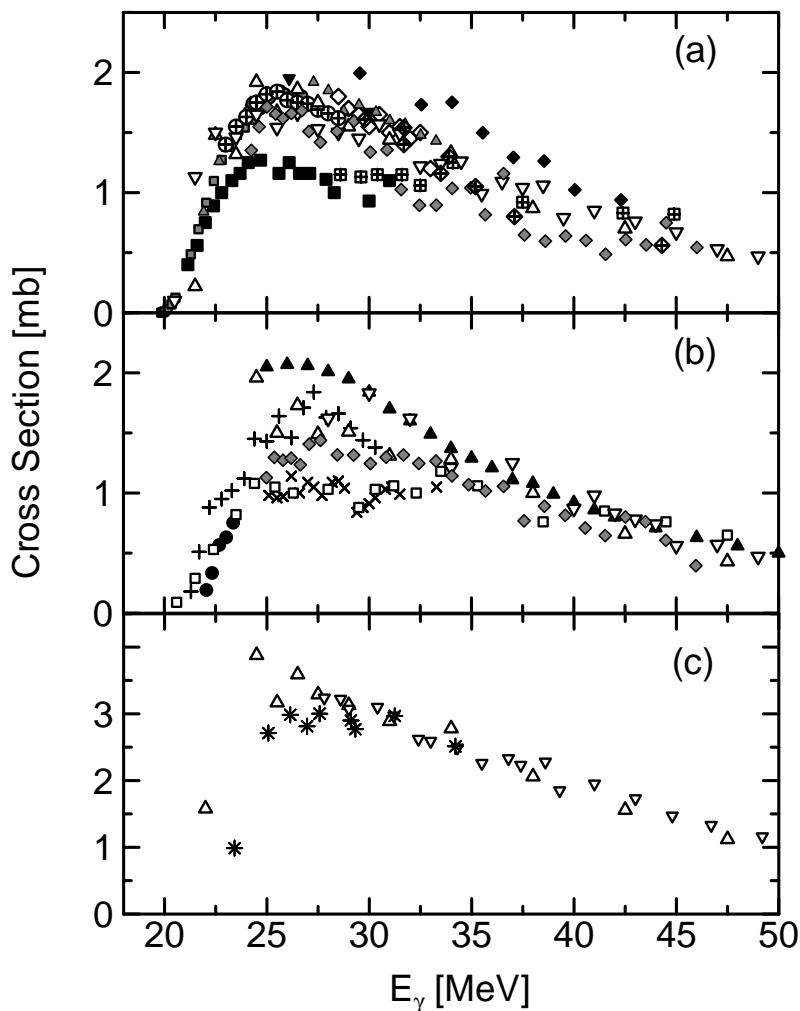


FIG. 1: Available data of the  ${}^4\text{He}$  photodisintegration cross sections: (a)  $(\gamma,p)$  cross sections, gray circles; Gardner *et al.* [13], crossed circles; Gemmell *et al.* [14], open upward triangles; Gorbunov [25], gray triangles; Meyerhof *et al.* [15], open downward triangles; Arkatov *et al.* [27], gray diamonds; Balestra *et al.* [29], filled diamonds; McBroom *et al.* [16], filled downward triangles; Calarco *et al.* [17], crossed squares; Bernabei *et al.* [11], filled squares; Feldman *et al.* [18], open diamonds; Hoorebeke *et al.* [12], gray squares; Hahn *et al.* [19], (b)  $(\gamma,n)$  cross sections, open upward triangles; Gorbunov [25], crosses; Irish *et al.* [20], filled upward triangles; Malcom *et al.* [21], open squares; Berman *et al.* [22], open downward triangles; Arkatov *et al.* [27], gray diamonds; Balestra *et al.* [29], diagonal crosses; Ward *et al.* [23], filled circles; Komar *et al.* [24], (c) total photoabsorption cross sections, open upward triangles; Gorbunov *et al.* [26], open downward triangles; Arkatov *et al.* [27], asterisks; Wells *et al.* [31]. The error bars are not shown for clarity.

multaneous ratio measurements for the  ${}^4\text{He}(\gamma,p){}^3\text{H}$  and  ${}^4\text{He}(\gamma,n){}^3\text{He}$  channels. Hence, one can hardly discuss the validity of the charge symmetry of the strong nuclear force using existing data. Hence it is highly required to accurately measure these cross sections with use of a new method in the GDR region, in particular between 22 and 32 MeV [11, 12, 31, 42].

In designing a new experiment, it would be worthwhile to reconsider what we learned from previous data. Firstly, we notice that both the  ${}^4\text{He}(\gamma,p){}^3\text{H}$  and  ${}^4\text{He}(\gamma,n){}^3\text{He}$  cross sections measured with bremsstrahlung photons are much larger than those measured with monoenergetic photons in the energy

range from 22 to 30 MeV, and they agree with each other above  $\sim 35$  MeV. Theoretically the two-body as well as the total cross sections are well described by a plane-wave approximation and they agree with previous data above 50 MeV [5]. Secondly, most experiments were performed separately for the  ${}^4\text{He}(\gamma,p){}^3\text{H}$  and  ${}^4\text{He}(\gamma,n){}^3\text{He}$  channels via the photodisintegration reactions and/or the inverse nucleon capture reactions. Thirdly, the simultaneous two-body and three-body cross section measurements were performed using a cloud chamber, which did not allow us to take data in an event-by-event mode with a pulsed photon beam, which is necessary to reject background. One may conclude that the large discrepancies

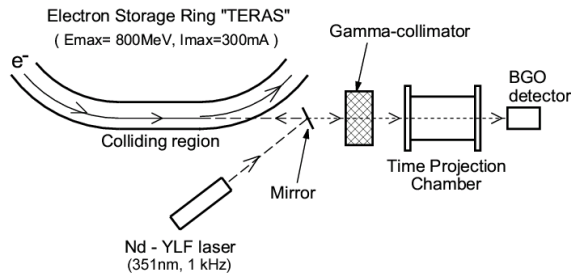


FIG. 2: Experimental setup for measurement of the photo-disintegration of  ${}^4\text{He}$  at AIST.

between different data sets could be due to background inherent to incident photon beams and/or due to an uncertainty of the normalization of the  ${}^4\text{He}(\gamma, p){}^3\text{H}$  and  ${}^4\text{He}(\gamma, n){}^3\text{He}$  cross sections.

In the present study we have carried out the simultaneous measurement of the two-body and three-body  ${}^4\text{He}$  photodisintegration cross sections in the energy region between 21.8 and 29.8 MeV using a monoenergetic pulsed laser Compton backscattering photon beam by means of a newly developed  $4\pi$  time projection chamber containing  ${}^4\text{He}$  gas as an active target.

## II. EXPERIMENT

### A. Experimental method

The experiment was carried out using a pulsed Laser Compton backscattering (LCS) photon beam at the National Institute of Advanced Industrial Science and Technology (AIST). The charged fragments from the photodisintegration of  ${}^4\text{He}$  were detected by means of a time projection chamber (TPC). A schematic view of an experimental setup is shown in Fig. 2.

A quasi-monoenergetic pulsed LCS photon beam was produced via the Compton backscattering of the photons from a Nd:YLF laser in third harmonics ( $\lambda = 351$  nm) with electrons circulating in the 800 MeV storage ring TERAS at the AIST [34]. An LCS photon beam is well known to be an excellent probe to measure a photodisintegration cross section of a nucleus with little background associated with primary photon beam and with small uncertainty in determination of the LCS photon flux using a  $\gamma$ -ray detector. Even with this kind of setup, there are several difficulties inherent to the measurement of the photodisintegration cross section of  ${}^4\text{He}$ , among which the cross section is small (about  $\sim 1$  mb), the photon beam flux is low, the target density of  ${}^4\text{He}$  is low, and the energies of the fragments from the photodisintegration of  ${}^4\text{He}$  in the GDR region are quite low, typically less than a few MeV. Hence, it has been crucial to develop a new detector, which enabled us to make a simultaneous measurement of the two-body and three-body photodisintegration cross sections of  ${}^4\text{He}$  by detecting such a low

energy fragment with an efficiency of 100% with a large solid angle of  $4\pi$ , and with a large signal-to-noise ratio.

In the present study we constructed a TPC which meets the mentioned requirements.

### B. Laser Compton backscattering (LCS) photon beam

A pulsed LCS  $\gamma$ -ray with the maximum energies  $E_{max} = 22.3, 25, 28$  and  $32$  MeV was used in the present experiment, obtained by changing the electron energy of the TERAS. The pulse width of the electron beam was 6 ns with a repetition rate of 100 MHz, while that of the laser photon beam was 150 ns with a repetition rate of 1 kHz. Pulsed laser photons scattered by electrons were collimated using a lead block with a hole of 2 mm in diameter and 200 mm in length to obtain quasi-monoenergetic LCS  $\gamma$ -rays. The absolute value of  $E_{max}$  was determined with accuracy better than 1% from the wavelength of the laser light and the kinetic energy of the electron beam. The electron beam energy has been calibrated by measuring the LCS  $\gamma$ -ray energy generated with Nd:YAG laser photons in fundamental mode ( $\lambda = 1064$  nm) [34]. The half-width of the  $\gamma$ -ray energy distribution was 2.5 MeV at  $E_{max} = 32$  MeV, and the obtained  $\gamma$ -ray intensity was about  $10^4$  photons/s. The TPC was placed 3 m downstream of the lead collimator.

### C. Time projection chamber (TPC)

A  $4\pi$  time projection chamber containing  ${}^4\text{He}$  gas as an active target was constructed to detect the charged fragments from the photodisintegration of  ${}^4\text{He}$  with an efficiency of 100%. The TPC was contained in a vessel with a size of 244 mm in inner diameter and 400 mm in length. A mixed gas of 80% natural He and 20%  $\text{CH}_4$  with a total pressure of 1000 Torr was filled in the vessel as a target for the photon-induced reactions and an operational gas of the TPC.

The TPC consisted of a drift region with a uniform electric field with an area of  $60 \times 60$  mm<sup>2</sup> and a length of 250 mm, and a multi-wire proportional counter (MWPC) region as shown in Fig. 3. The MWPC consisted of one anode plane and two cathode planes, which were set with a gap of 2 mm. Each plane had 30 wires with a spacing of 2 mm. In order to obtain two-dimensional track information of a charged fragment, cathode wires in front of and behind the anode plane were stretched along x- and y-axes, respectively. Here the x- and y-directions were defined to be parallel to and perpendicular to the anode wires, respectively.

The TPC operates as follows. Electrons were produced by the interaction of a charged fragment with the mixed gas along the fragment path in the drift region. The electrons were drifted along the uniform electric field toward the MWPC region, where they were multiplied via an

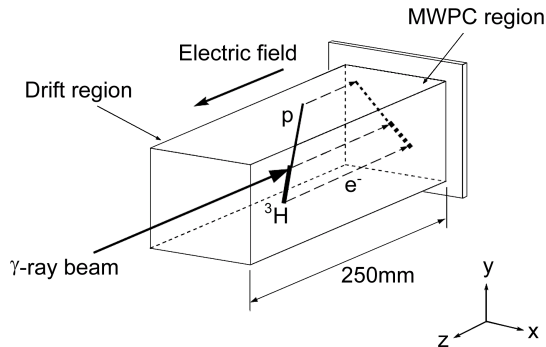


FIG. 3: Schematic drawing of the structure of the TPC.

avalanche process. The avalanche signal was picked up with both the anode- and cathode-wires. The cathode signals were used to measure the track of a charged fragment on an x-y plane, since the directions of these cathode wires were perpendicular to each other. A z-position of a charged fragment was determined by measuring the drift time of the electrons with use of a time to digital converter as described below. An anode signal was used to determine the amount of energy loss of a fragment in the drift region of the TPC. Both, track and energy loss signals of a charged fragment were used to clearly identify a reaction channel. It should be noted that since a light charged fragment did not stop in the drift region, we observed various energy loss signals depending on a charged fragment type and on incident LCS  $\gamma$ -ray energy. An external magnetic field has not been used in the present TPC configuration.

The performance of the TPC was studied using the  $^{241}\text{Am}$   $\alpha$ -ray source and a Si detector. The energy resolution of the TPC was measured as being 7.5% (FWHM) per anode wire. Since the energy measured by an anode wire depends on the emission angle of a fragment with respect to the anode wire direction, we collimated an  $\alpha$ -ray and determined its emission angle by using a coincidence signal between the TPC anode signal and the signal from the Si detector. A drift velocity of ionized electrons was measured as a function of the z-position using the same measuring system. A typical value of the drift velocity was  $7.00 \pm 0.14$  mm/ $\mu$ s. The time resolution was obtained as being 32 ns ( $1\sigma$ ), which corresponded to the position resolution along the z-direction of 0.22 mm ( $1\sigma$ ). Detailed description of the TPC will be published elsewhere [35].

#### D. Electronics and data acquisition

A schematic diagram of data acquisition system is shown in Fig. 4. A linear signal from the preamplifier was used as a stop signal for a time to digital converter (TDC) after discriminating the electronic noise by a com-

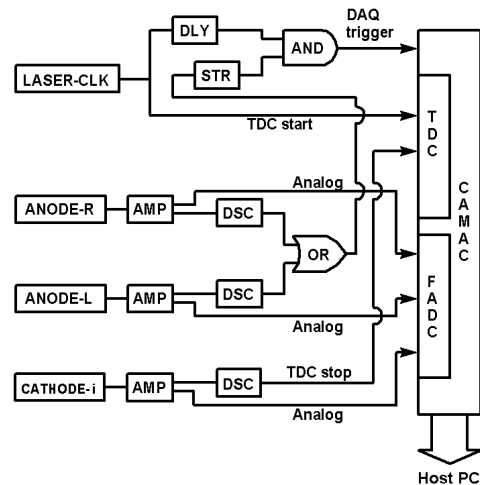


FIG. 4: Block diagram of the data acquisition system. LASER-CLK; laser clock pulse, ANODE-R(L); sum of the linear signals from the anode wires in right- (left-) hand side with respect to the LCS photon beam axis, CATHODE-i; linear signal from the i-th cathode wire, AMP; preamplifier, DSC; discriminator, DLY; delay circuit, and STR; pulse stretcher.

parator. A common start signal for the TDC is obtained from the output of a pulsed laser clock. Both times, the leading edge and the trailing edge of an input signal are recorded on the TDC not only to determine the drift time of electrons but also to unambiguously identify the reaction channel. To measure the amount of energy loss of a charged fragment by integrating the current of a signal, we recorded its pulse shape using a flash ADC (FADC) and constructed a charge-integrated spectrum of a fragment in the off-line analysis.

Concerning the data acquisition, a trigger signal for the TPC is obtained from the clock pulse of the laser system. A logic signal from a cathode wire is sent to a discriminator to reject the noise signal and then sent to the TDC to measure a drift time of ionized electrons. An anode signal is used to generate a TPC-hit signal. When a 70  $\mu$ s delayed signal of the laser clock pulse and the TPC-hit signal are in coincidence within a gate width of 100  $\mu$ s, the data are acquired. The width is set longer than the maximum drift time (36  $\mu$ s) of electrons in the TPC drift region in order to measure not only the photodisintegration event of  $^4\text{He}$  but also background events. Data from CAMAC modules are acquired by a personal computer and recorded on a hard disk drive in an event-by-event mode. The TPC count rate during the experiment was several tens of counts per second, and thus the dead time of the data taking system was a few % (monitored during the measurement). A PC-based pulse-height analyzer was used for monitoring the LCS  $\gamma$ -ray intensities with a BGO detector as described below.

### III. ANALYSIS AND RESULTS

#### A. Event identification

All pulse-height spectra taken by the FADC were analyzed to classify the observed events into photodisintegration events of  $^4\text{He}$  and  $^{12}\text{C}$ , and background events. We observed  $^{12}\text{C}$  events, since we used  $\text{CH}_4$  gas. The total event rate in the present experiment was of several tens of counts per second, and the event rate from the photodisintegration of  $^4\text{He}$  and  $^{12}\text{C}$  was of several tens of counts per hour, less than one thousandth of the background events. A detailed description of electron background, natural background and photodisintegration events is given here below.

##### 1. Background events

(1) *Electron events.* Most events taken by the FADC were due to background. The dominant background was originating from the interaction of LCS  $\gamma$ -rays with atomic electrons of  $^4\text{He}$  and  $\text{CH}_4$  used for the TPC. Electron events were identified by their small pulse height. Note that electron energy loss rate in the TPC was small, of the order of 0.1 keV/mm, since electron energy was in the range from a few MeV to several tens of MeV. Therefore most electron events could be discriminated by a discriminator. A typical spectrum taken by the FADC is shown in Fig. 5. Here a dotted line indicates a threshold level, which was set to further remove electron background during the off-line analysis. Typical tracks of electron events, which were detected with one anode trigger signal and whose energies were above the threshold level, are shown in Fig. 6. Note that we could see several tracks for one anode trigger signal. In addition, observed tracks were not straight, seldom crossed the LCS  $\gamma$ -ray axis, and their track width was quite thin. These features allowed us to unambiguously identify electron events.

(2) *Natural background events.* The natural background events are not correlated with the pulsed LCS  $\gamma$ -rays, and therefore the track did not cross the LCS  $\gamma$ -ray axis as shown in Fig. 7. Hence the natural background events could be clearly discriminated from the photodisintegration events of  $^4\text{He}$  and  $^{12}\text{C}$ . Since the track width of natural background is wider than that of electrons, the background might be due to an  $\alpha$ -particle from a natural radioactivity such as Rn contained in the TPC chamber or in the mixed gas of natural He and  $\text{CH}_4$ .

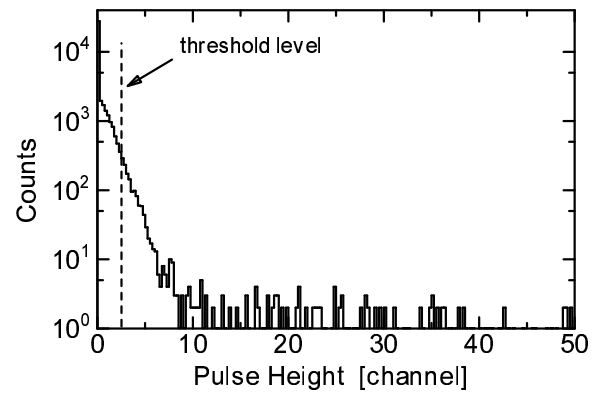


FIG. 5: Pulse-height spectrum for all the acquired events. The huge component below  $\sim 10$  ch is mainly due to scattered electrons.

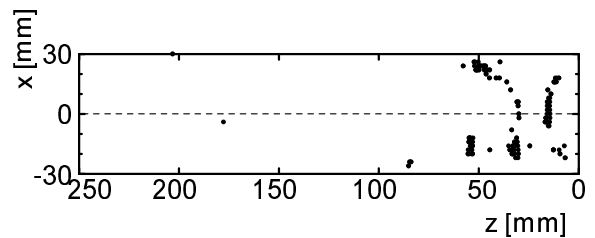


FIG. 6: Example of a track of a scattered electron. The  $\gamma$ -ray beam is coming from the left-hand side. The dots indicate the envelopes of the electron clouds ionized by the scattered electrons. The dashed line denotes the incident  $\gamma$ -ray beam axis. The box is the drift region of the TPC (side view).

##### 2. Photodisintegration events of $^4\text{He}$ and $^{12}\text{C}$

Both electron and natural background events were identified as described above. Consequently, the background free (BF) events, which contained the photodisintegration events of  $^4\text{He}$  and  $^{12}\text{C}$ , were obtained from all the events recorded on the FADC. We checked the path length, the track width and the pulse height of each BF event to finally identify a reaction channel for the photodisintegration of  $^4\text{He}$  and  $^{12}\text{C}$ .

The calculated path length of the various fragments from the photodisintegration of  $^4\text{He}$  and  $^{12}\text{C}$  in the present experiment are listed in Table I. The path length

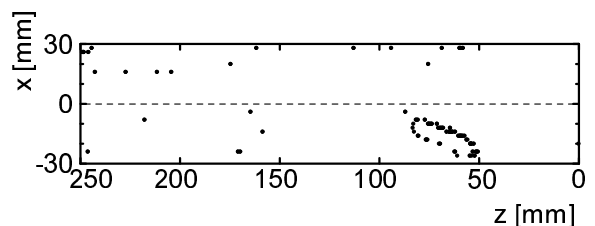


FIG. 7: Example of a track of a natural background event.

TABLE I: Maximum ranges of the fragments from the photodisintegrations of  ${}^4\text{He}$  and  ${}^{12}\text{C}$  (unit:mm).

Reaction channel	Q [MeV]	Fragment	$E_\gamma$ [MeV]			
			22.3	25	28	32
${}^4\text{He}(\gamma,\text{p}){}^3\text{H}$	-19.81	p	130	580	1310	2690
		${}^3\text{H}$	14.5	45	91	174
${}^4\text{He}(\gamma,\text{n}){}^3\text{He}$	-20.58	${}^3\text{He}$	6	17	58	135
${}^4\text{He}(\gamma,\text{pn}){}^2\text{H}$	-26.07	p	–	–	84	590
		${}^2\text{H}$	–	–	34	214
${}^{12}\text{C}(\gamma,\text{p}){}^{11}\text{B}$	-15.96	p	1080	2230	3770	6440
		${}^{11}\text{B}$	4.3	6	7	9
${}^{12}\text{C}(\gamma,\text{n}){}^{11}\text{C}$	-18.72	${}^{11}\text{C}$	3	4.3	5.5	7.4

of a light fragment such as p,  ${}^3\text{H}$  and  ${}^3\text{He}$  is much longer than that of a heavy fragment such as  ${}^{11}\text{B}$  and  ${}^{11}\text{C}$ . Hence, the photodisintegration of  ${}^4\text{He}$  can be separated from that of  ${}^{12}\text{C}$  by referring to the path length of a charged fragment.

The track width of a charged fragment was obtained by converting both times of the leading edge and the trailing edge of a cathode signal into the z-coordinate of the fragment track. Note that as the pulse height of a cathode signal becomes higher, the time difference between these two edges is larger, and thus the track width becomes wider. Hence, the track width of a charged fragment provides energy loss information of a fragment in the TPC. Since the energy loss rate of a fragment depends on the fragment type (p,  ${}^2\text{H}$ ,  ${}^3\text{H}$ ,  ${}^3\text{He}$ ,  ${}^4\text{He}$ ,  ${}^{11}\text{B}$ , and  ${}^{11}\text{C}$ ), the track width of a fragment was used to identify its photodisintegration reaction channel together with the path length, the charge-integrated pulse height taken by the FADC and the reaction kinematics.

The measured pulse height spectrum of a fragment was compared to the spectrum calculated by a Monte-Carlo method. The Monte-Carlo calculation simulated the kinematics of the photodisintegration events, the migration of drift electrons, and the pulse shapes of the signals from the anode and cathode wires. The calculation has been performed as follows. Firstly, an incident intrinsic LCS photon spectrum of given energy was generated which reproduced a measured energy spectrum with a NaI(Tl) detector. Then, a reaction point was randomly chosen in the region irradiated by the LCS photon beam in the TPC. The track of a charged fragment emitted by a photodisintegration reaction of  ${}^4\text{He}$  and/or  ${}^{12}\text{C}$  was calculated by considering the LCS photon energy and the Q-value of the reaction. In order to calculate the emission angle of a charged fragment we assumed an E1 angular distribution and an isotropic distribution for the two-body and three-body channels of the photodisintegration of  ${}^4\text{He}$ , respectively. Note that the E1 dominance of the two-body channel was experimentally shown as mentioned above [16, 17, 32], and the isotropic fragment distribution was also observed for the  $\gamma$ -ray energy range from 28 to 60 MeV within the experimental uncertainty [26, 28, 30]. The energy

deposited by a charged fragment was calculated as a function of the distance from a reaction point using the energy loss formula given by Ziegler *et al.* [36], and was converted to the number of ionized electrons using the ionization energy of electrons in the TPC gas. The drift time of ionized electrons was calculated using the local drift velocity, which has been obtained as a function of the electric field strength in the TPC as described above. Using the drift time thus calculated, the shaping time of an amplifier, and the threshold level of a discriminator, we obtained the simulated data of FADC and TDC for each wire. The event data thus obtained were recorded and analyzed with the same procedure as for the data of the real measurements.

(1) *Two-body channel of  ${}^4\text{He}$  photodisintegration.* This channel is characterized by the fact that two fragments p (n) and  ${}^3\text{H}$  ( ${}^3\text{He}$ ) are emitted in the opposite direction with respect to the LCS  $\gamma$ -ray beam direction, with equal momentum in the center-of-mass system. This channel can be separated from the two-body channel of  ${}^{12}\text{C}$  disintegration by the completely different path lengths of the charged fragments as mentioned above.

(i)  ${}^4\text{He}(\gamma,\text{p}){}^3\text{H}$  channel

Both the proton and the triton were detected by the TPC. An event, which meets the reaction kinematics conditions mentioned above, is selected as a candidate event of the  ${}^4\text{He}(\gamma,\text{p}){}^3\text{H}$  event. Since the energy loss of  ${}^3\text{H}$  is a few times larger than that of a proton, the track width of  ${}^3\text{H}$  is wider than that of a proton. A typical track of an event observed at  $E_{max} = 28$  MeV consistent with the above-mentioned feature is shown in Fig. 8(a). The sum spectrum of the measured pulse height of p and of  ${}^3\text{H}$  is in good agreement with that of a Monte-Carlo simulation as shown in Fig. 8(b). This event can be unambiguously assigned as a  ${}^4\text{He}(\gamma,\text{p}){}^3\text{H}$  event.

(ii)  ${}^4\text{He}(\gamma,\text{n}){}^3\text{He}$  channel

The TPC was not sensitive to neutrons, and therefore only the  ${}^3\text{He}$ , which crossed the LCS  $\gamma$ -ray axis, was detected for this reaction channel. A typical track of the event observed at  $E_{max} = 28$  MeV is shown in Fig. 9(a). The track of  ${}^3\text{He}$  is shown to extend to the opposite side across the central axis of the TPC. This is due to the finite size of the LCS photon beam and the diffusion of secondary electrons during the migration to the MWPC. The pulse height spectrum of  ${}^3\text{He}$  agrees nicely with a simulated one as shown in Fig. 9(b). Note that the track length of  ${}^3\text{He}$  is much longer compared to that of  ${}^{11}\text{C}$  as shown in Fig. 10 (also Fig. 12(a)), and therefore the  ${}^4\text{He}(\gamma,\text{n}){}^3\text{He}$  events can be clearly separated from the  ${}^{12}\text{C}(\gamma,\text{n}){}^{11}\text{C}$  events.

(iii)  ${}^4\text{He}(\gamma,\text{d}){}^2\text{H}$  channel

We did not observe any candidate of the  ${}^4\text{He}(\gamma,\text{d}){}^2\text{H}$  reaction. Note that the  ${}^4\text{He}(\gamma,\text{d}){}^2\text{H}$  cross section was

measured to be about  $3.2 \mu\text{b}$  at the peak of  $E_\gamma = 29 \text{ MeV}$  [37], and it is therefore much smaller compared to the  ${}^4\text{He}(\gamma, p){}^3\text{H}$  and  ${}^4\text{He}(\gamma, n){}^3\text{He}$  cross sections (a few mb at the corresponding  $\gamma$ -ray energy).

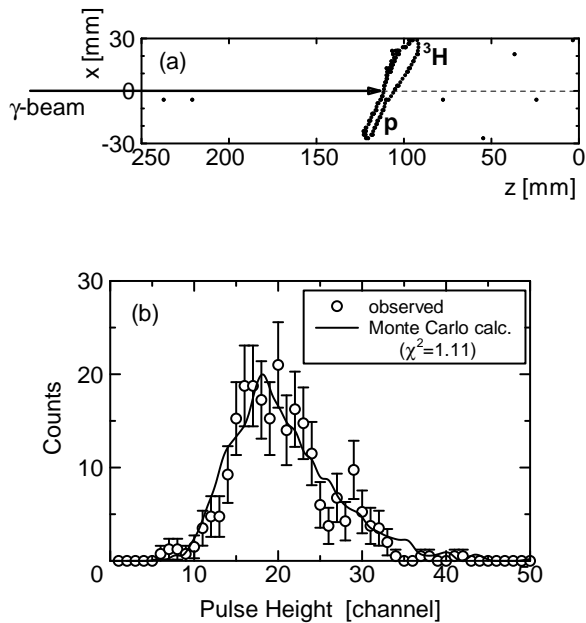


FIG. 8: (a) Example of the  ${}^4\text{He}(\gamma, p){}^3\text{H}$  event. (b) Total pulse height spectrum of the  ${}^4\text{He}(\gamma, p){}^3\text{H}$  reaction: open circles; observed, solid curve; fitting spectrum calculated with a Monte-Carlo simulation.

(2) *Two-body channel in the  ${}^{12}\text{C}$  photodisintegration.* This channel is characterized by the fact that two fragments p (n) and  ${}^{11}\text{B}$  ( ${}^{11}\text{C}$ ) are emitted in the opposite direction with respect to the LCS  $\gamma$ -ray beam axis with equal momentum in the center-of-mass system. The path length of  ${}^{11}\text{B}$  and  ${}^{11}\text{C}$ , however, are much shorter than that of  ${}^3\text{H}$  and  ${}^3\text{He}$ , and therefore this two-body channel can be clearly separated from that of  ${}^4\text{He}$ .

(i)  ${}^{12}\text{C}(\gamma, p){}^{11}\text{B}$  channel

Both the proton and  ${}^{11}\text{B}$  are detected by the TPC. A typical track of an event which meets the above-mentioned condition, observed at  $E_{max} = 28 \text{ MeV}$ , is shown in Fig. 11(a). The path length of the proton is much longer than that of  ${}^{11}\text{B}$ , and the track width of the proton is much narrower than that of  ${}^{11}\text{B}$ . The sum spectrum of the measured pulse height of  ${}^{11}\text{B}$  and p is in good agreement with the Monte-Carlo simulation as shown in Fig. 11(b).

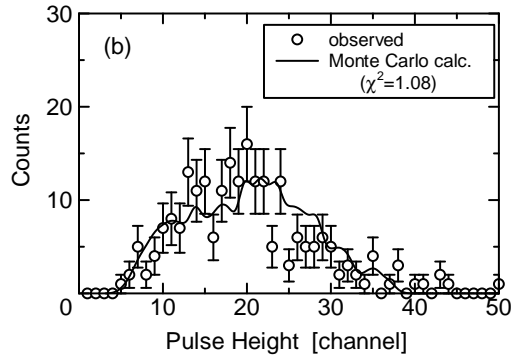
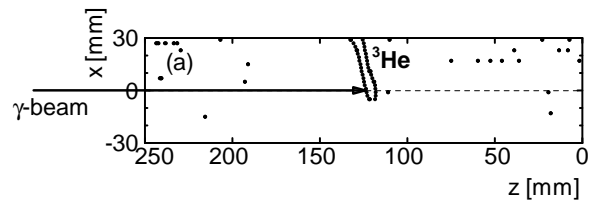


FIG. 9: (a) Example of the  ${}^4\text{He}(\gamma, n){}^3\text{He}$  event. (b) Total pulse height spectrum of the  ${}^4\text{He}(\gamma, n){}^3\text{He}$  reaction.

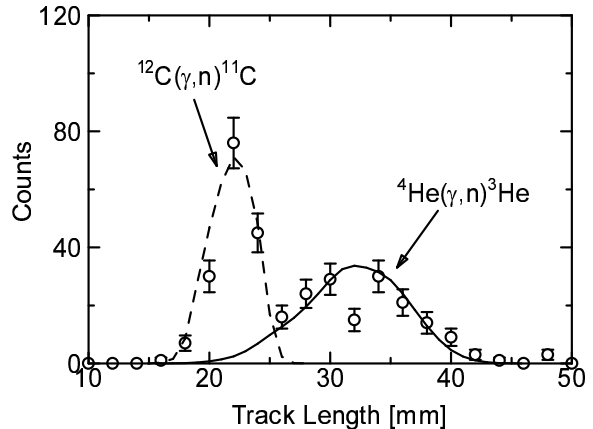


FIG. 10: Distributions of the track length of charged fragments from the  ${}^4\text{He}(\gamma, n){}^3\text{He}$  and  ${}^{12}\text{C}(\gamma, n){}^{11}\text{C}$  reactions observed for  $E_{max} = 28 \text{ MeV}$ . The open circles are the experimental data. The solid curve and the dashed curve are the results of Monte-Carlo simulations for  ${}^4\text{He}(\gamma, n){}^3\text{He}$  and  ${}^{12}\text{C}(\gamma, n){}^{11}\text{C}$ , respectively.

(ii)  ${}^{12}\text{C}(\gamma, n){}^{11}\text{C}$  channel

Only the track of  ${}^{11}\text{C}$ , which crossed the LCS  $\gamma$ -ray beam axis, was observed for this reaction channel. A typical track of a  ${}^{12}\text{C}(\gamma, n){}^{11}\text{C}$  event observed at  $E_{max} = 28 \text{ MeV}$  is shown in Fig. 12(a). The path length of  ${}^{11}\text{C}$  is much shorter than that of  ${}^3\text{He}$  as shown in Fig. 10, and therefore we could unambiguously discriminate the  ${}^{12}\text{C}(\gamma, n){}^{11}\text{C}$  events from those of the  ${}^4\text{He}(\gamma, n){}^3\text{He}$  reaction. The pulse height spectrum of  ${}^{11}\text{C}$  also agrees nicely with the simulated one as shown in Fig. 12(b).



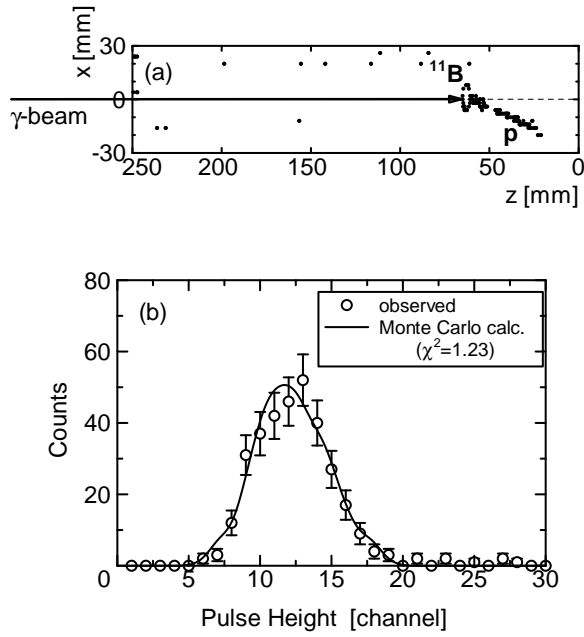


FIG. 11: (a) Example of the  $^{12}\text{C}(\gamma,p)^{11}\text{B}$  event. (b) Total pulse height spectrum of the  $^{12}\text{C}(\gamma,p)^{11}\text{B}$  reaction.

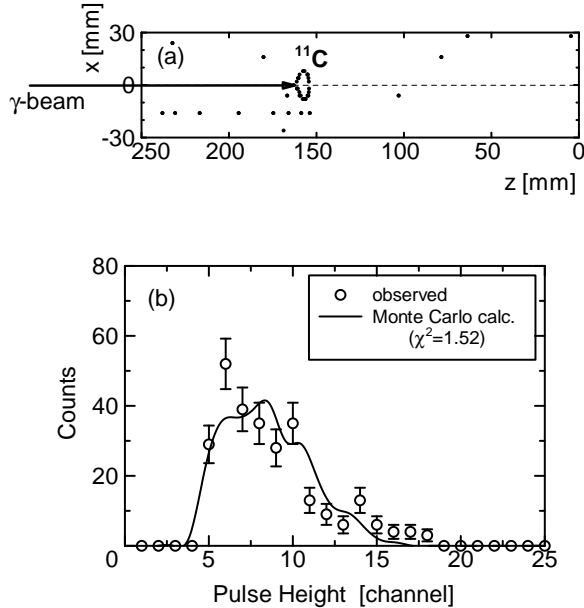


FIG. 12: (a) Example of the  $^{12}\text{C}(\gamma,n)^{11}\text{C}$  event. (b) Total pulse height spectrum of the  $^{12}\text{C}(\gamma,n)^{11}\text{C}$  reaction.

### (3) Three-body channels.

#### (i) $^4\text{He}(\gamma,pn)^2\text{H}$ channel

The Q-value of the  $^4\text{He}(\gamma,pn)^2\text{H}$  reaction is -26.1 MeV, and therefore the reaction events could only be observed at  $E_{max} = 28$  and 32 MeV. This reaction event can be discriminated from that of the  $^4\text{He}(\gamma,p)^3\text{H}$  reaction, because the tracks of the proton and deuteron are randomly oriented with respect to one another in the center-of-mass system and with respect to the LCS  $\gamma$ -ray beam axis, and the path length of the proton from the  $^4\text{He}(\gamma,pn)^2\text{H}$  reaction is much shorter than that of the  $^4\text{He}(\gamma,p)^3\text{H}$  reaction. A typical track of p and  $^2\text{H}$  observed at  $E_{max} = 28$  MeV is shown in Fig. 13. In this case, the track width of the proton is not constant and depends on the proton energy.

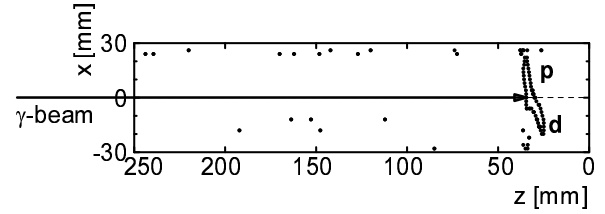


FIG. 13: Example of the  $^4\text{He}(\gamma,pn)^2\text{H}$  three-body event.

#### (ii) $^{12}\text{C}(\gamma,2\alpha)^4\text{He}$ channel

This reaction event can be easily identified by three tracks of the particles as shown in Fig. 14, which was observed at  $E_{max} = 28$  MeV.

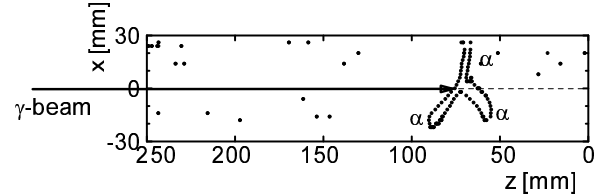


FIG. 14: Example of the  $^{12}\text{C}(\gamma,2\alpha)^4\text{He}$  event.

(4) *Photodisintegration reaction of  $^4\text{He}$  and/or  $^{12}\text{C}$  without LCS photon beams.* We checked for possible photodisintegration events of  $^4\text{He}$  and/or  $^{12}\text{C}$  caused by bremsstrahlung photons from the TERAS, but not LCS photons. Since such an event would occur continuously, the data corresponding to the drift time of between 40 and 64  $\mu\text{s}$  were analyzed. We did not find any event which could be identified as any of the reaction channels of the photodisintegrations of  $^4\text{He}$  and/or  $^{12}\text{C}$ .

## B. Cross sections of the photodisintegrations of ${}^4\text{He}$ ( $\sigma_i(E_\gamma)$ )

The incident LCS  $\gamma$ -ray has a finite energy spread, and the TPC efficiency depends on the incident  $\gamma$ -ray energy as described below. Hence, a partial cross section  $\sigma_i(E_\gamma)$  corresponding to the two-body and/or the three-body photodisintegration of  ${}^4\text{He}$  at a  $\gamma$ -ray energy  $E_\gamma$  is given as follows:

$$Y_i = N_t \cdot L \cdot \Phi \times \frac{\int_0^{E_{max}} \varepsilon_i(E_\gamma) \cdot \sigma_i(E_\gamma) \cdot \phi(E_\gamma) dE_\gamma}{\int_0^{E_{max}} \phi(E_\gamma) dE_\gamma}. \quad (1)$$

Here  $Y_i$ ,  $N_t$  and  $L$  stand for the yield of a reaction channel  $i$ , the number density of the target nuclei, and the effective length of the TPC, respectively.  $E_{max}$  denotes the maximum energy of the incident LCS  $\gamma$ -ray. The parameter  $\varepsilon_i(E_\gamma)$  is the detection efficiency of the TPC for a fragment emitted by the photodisintegration process at the  $\gamma$ -ray energy  $E_\gamma$ . The parameter  $\phi(E_\gamma)$  denotes the intensity of the incident LCS  $\gamma$ -ray at the energy  $E_\gamma$ .  $\Phi$  is the incident LCS  $\gamma$ -ray flux, and is equal to the energy-integrated value of  $\phi(E_\gamma)$ . The average cross section  $\langle \sigma_i \rangle$  and the weighted-mean reaction energy  $\langle E_\gamma \rangle_i$  are defined as

$$\begin{aligned} \langle \sigma_i \rangle &= \frac{\int_0^{E_{max}} \varepsilon_i(E_\gamma) \cdot \sigma_i(E_\gamma) \cdot \phi(E_\gamma) dE_\gamma}{\int_0^{E_{max}} \varepsilon_i(E_\gamma) \cdot \phi(E_\gamma) dE_\gamma} \\ &= \frac{Y_i}{N_t \cdot L \cdot \int_0^{E_{max}} \varepsilon_i(E_\gamma) \cdot \phi(E_\gamma) dE_\gamma}, \quad (2) \end{aligned}$$

$$\langle E_\gamma \rangle_i = \frac{\int_0^{E_{max}} E_\gamma \cdot \varepsilon_i(E_\gamma) \cdot \sigma_i(E_\gamma) \cdot \phi(E_\gamma) dE_\gamma}{\int_0^{E_{max}} \varepsilon_i(E_\gamma) \cdot \sigma_i(E_\gamma) \cdot \phi(E_\gamma) dE_\gamma}. \quad (3)$$

The parameters  $\varepsilon_i$ ,  $N_t$ ,  $L$ ,  $\Phi$  and  $\phi$  were determined as discussed in the following subsections.

### 1. Effective length ( $L$ ) and detection efficiency ( $\varepsilon_i(E_\gamma)$ ) of the TPC

Any charged fragments produced by the photodisintegration of  ${}^4\text{He}$  and/or  ${}^{12}\text{C}$  in the TPC produces electrons by interacting with atomic electrons in the He and  $\text{CH}_4$  mixed gas in the TPC. Since the signal of an electron is picked up by the anode and the cathode wires, the efficiency  $\varepsilon_i(E_\gamma)$  of the TPC is expected to be as high as 100% along the TPC geometrical drift length of 250 mm. However, since the electric field strength applied in the drift region is not uniform at both edges of the drift region, the efficiency is not constant in the whole length of the drift region. Hence, we measured a pulse height spectrum of  $\alpha$ -particles from the decay of  ${}^{241}\text{Am}$  to determine an effective length  $L$ , in which a pulse height was constant to provide a constant efficiency. The length

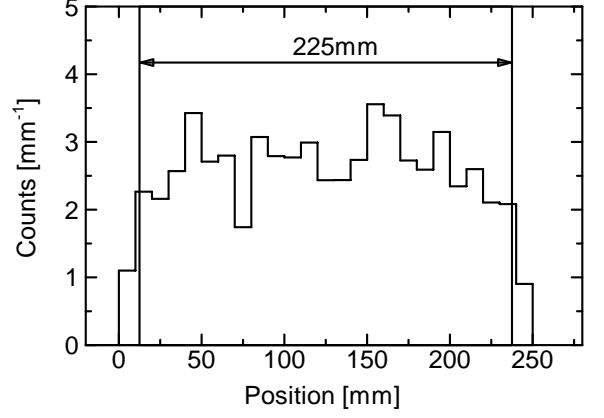


FIG. 15: Position distribution of the  ${}^4\text{He}$  photodisintegration yield along the z-direction.

$L$  is defined as 225 mm in the region between  $z = 12.5$  mm and 237.5 mm. Fig. 15 shows the position distribution of the photodisintegration event of  ${}^4\text{He}$  along the z-direction. It is clearly seen that the distribution is uniform within the effective length within the experimental uncertainty.

One might expect a 100% efficiency  $\varepsilon_i(E_\gamma)$  within the effective length. However since the energy of a fragment from the photodisintegration of  ${}^4\text{He}$  and/or  ${}^{12}\text{C}$  is low and discriminators were used to reject electric noise of both the anode and cathode signals and electron background, it is necessary to investigate a possible change of the efficiency due to threshold levels of the discriminators of the cathode and anode signals.

It should be mentioned that the anode signal was obtained by summing signals from several anode wires on either right-hand side or left-hand side with respect to the LCS  $\gamma$ -ray beam axis as shown in the block diagram of the data acquisition system in Fig. 4. Since the average energy deposit by a charged fragment from the photodisintegration is above 500 keV, an average pulse height of the summed anode signal is above 500 keV. A threshold level of the anode signal was set at about 5 keV by referring to the  $\alpha$ -ray pulse height spectrum of  ${}^{241}\text{Am}$  not to decrease the efficiency.

On the other hand, a cathode signal was obtained from each cathode wire as shown in Fig. 4. A threshold level of the cathode signal was set at about 0.8 keV, and the effect of the discriminator on the efficiency was studied by making a pulse peak height spectrum of its signal. The spectrum was obtained by taking the maximum peak of all signals of a cathode wire taken by FADC. A typical spectrum for a proton and a  ${}^3\text{H}$  from the  ${}^4\text{He}(\gamma, p){}^3\text{H}$  channel is respectively shown in Fig. 16, where a solid curve indicates a peak height spectrum calculated by a Monte-Carlo method, and the dotted line is the threshold level set in the present measurement. The measured peak height spectrum is in good agreement with the simulated one both for the proton as well as for the  ${}^3\text{H}$ . Since the

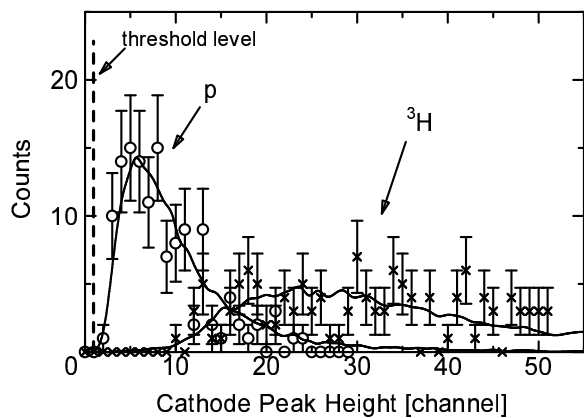


FIG. 16: Peak pulse-height spectra of proton (open circles) and  $^3\text{H}$  (diagonal crosses) from the  $^4\text{He}(\gamma, p)^3\text{H}$  reaction at  $E_{max} = 28$  MeV. Solid curves are the spectra calculated by a Monte-Carlo method.

pulse peak height of the proton is well above the threshold level, the discriminator for the cathode signal does not decrease the TPC efficiency. Using the Monte-Carlo simulation, the efficiency  $\varepsilon_i(E_\gamma)$  is obtained as being  $0.97(5) \sim 1.00(1)$  depending on the reaction energy. Here the bracket indicates the uncertainty of  $\varepsilon_i(E_\gamma)$ , which was obtained by fitting a measured pulse-height spectrum with the simulated one.

### 2. Target number density ( $N_t$ )

The target number density  $N_t$  was determined from measured pressure  $P$ , temperature  $T$  and chemical purity (99.999%) of the  $^4\text{He}$  gas in the TPC. The uncertainty in the determination of  $N_t$  was evaluated to be 0.18% due to the uncertainty in the determination of  $P$  and  $T$ .

### 3. Incident LCS $\gamma$ -ray flux ( $\Phi$ )

The incident LCS  $\gamma$ -rays were measured using a BGO detector with a diameter of 50.8 mm and a length of 152.4 mm. A typical measured  $\gamma$ -ray spectrum is shown in Fig. 17, in which we see multiple peaks due to pile-up effects.

The laser photon beam was pulsed with a pulse width of 150 ns and a repetition rate of 1 kHz, while the electron beam was also pulsed with a width of 6 ns and a repetition rate of 100 MHz. Laser photons, therefore, collide several times with electron bunches circulating in the TERAS within one long laser pulse width, and LCS  $\gamma$ -rays with the same energy distribution were produced within a time interval of 150 ns. Note that this time interval was too short for the BGO system to decompose the multiple LCS  $\gamma$ -rays into an individual LCS  $\gamma$ -ray produced by one electron pulse. Consequently, the multiple  $\gamma$ -ray peaks were produced as pile-ups in the LCS  $\gamma$ -ray spectrum (see Fig. 17).

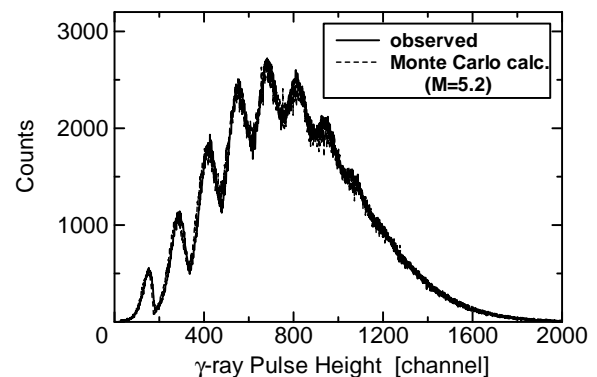


FIG. 17: Typical  $\gamma$ -ray pulse height spectrum for  $E_{max} = 28$  MeV. The solid curve and the dashed curve represent the measured one and the Monte-Carlo simulation assuming an average photon multiplicity  $M = 5.2$ , respectively.

The photodisintegration yield of  $^4\text{He}$  is proportional to an averaged number  $M$  of multiple LCS  $\gamma$ -rays per laser pulse. The number  $M$  was obtained by comparing a measured BGO spectrum to a calculated one obtained from a Monte-Carlo simulation [38]. The calculated spectrum was obtained with the following assumptions. The LCS  $\gamma$ -ray yield is proportional to the number of electrons (electron currents) times the number of laser photons. The probability density for generating LCS  $\gamma$ -rays per laser pulse is so small that the LCS  $\gamma$ -ray yield can be assumed to follow a Poisson distribution. The electron beam in the TERAS can be assumed to be a continuous beam because its repetition rate is much higher than that of the laser photon beam. The observed multiple peaks of the LCS  $\gamma$ -ray spectrum are assumed to be the sum of the pulse height spectra of each LCS  $\gamma$ -ray. This assumption is reasonable since the BGO responds to each  $\gamma$ -ray independently. The response function of the BGO detector to the LCS  $\gamma$ -ray was obtained by measuring the  $\gamma$ -ray spectrum with low flux, which was free from multiple peaks. Finally, the pulse shape of the BGO detector for multiple LCS  $\gamma$ -rays was obtained using both the time distribution of the LCS  $\gamma$ -ray measured by a plastic scintillation counter and a shaping time of  $1 \mu\text{s}$  of an amplifier used for the BGO detector system. Based on these assumptions, a response function of the BGO detector with an averaged number  $M$  of multiple LCS  $\gamma$ -rays was calculated by a Monte-Carlo method, and the number  $M$  was obtained by fitting a measured spectrum with the multiple peaks with the calculated response function. A typical measured spectrum is in good agreement with the calculated one with  $M = 5.2$  as shown in Fig. 17.

Using the number  $M$  thus determined the LCS  $\gamma$ -ray total flux  $\Phi$  is obtained as follows:

$$\Phi = M \times f \times T_L. \quad (4)$$

Here  $f$  is a frequency of the laser pulse, and  $T_L$  is a live time of the measurement. A  $\gamma$ -ray flux thus obtained has

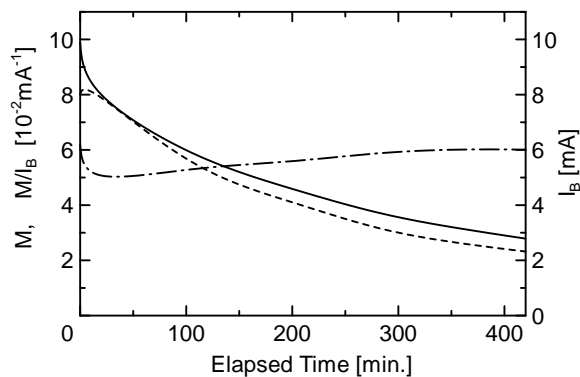


FIG. 18: Time dependences of the electron beam current  $I_B$  (dashed curve), the average photon number  $M$  (solid curve) and the photon production efficiency  $M/I_B$  (dash-dotted curve) for an electron beam current of 1 mA.

an uncertainty of about 2%, which consists of statistics of the LCS  $\gamma$ -ray yield, an uncertainty of the response function of the BGO detector, and an uncertainty in the least-square fitting of the LCS  $\gamma$ -ray spectrum with multiple peaks measured with the BGO detector.

It is interesting to see a relation between the electron current in the TERAS and the average number  $M$ , which is shown in Fig. 18. Electron currents are shown after electrons were injected into the TERAS. While an electron beam current gradually decreases due to the collision of electrons with the residual gas containing in the ring, the average number  $M$  remains almost constant.

#### 4. Energy spectrum of incident LCS $\gamma$ -ray ( $\phi(E_\gamma)$ )

To determine the photodisintegration cross section of  ${}^4\text{He}$  at a certain energy corresponding to an incident LCS  $\gamma$ -ray, it is necessary to measure the intrinsic energy spectrum  $\phi(E_\gamma)$  of incident LCS  $\gamma$ -rays. Note that the LCS  $\gamma$ -ray has a finite energy spread due to the finite widths of the lead collimator and of the emittance of electron beams of the TERAS. Hence the LCS  $\gamma$ -ray spectrum was measured using an anti-Compton NaI(Tl) spectrometer, which consisted of a central NaI(Tl) detector with a diameter of 76.2 mm and a length of 152.4 mm, and an annular one with an outer diameter of 254 mm and a length of 280 mm. A typical spectrum measured at  $E_{max} = 28$  MeV is shown in Fig. 19. Using a response function of the NaI(Tl) detector calculated with the GEANT4 simulation code [39], the intrinsic energy spectrum of the LCS  $\gamma$ -ray was obtained as shown in Fig. 19. An energy spread of LCS  $\gamma$ -rays was determined as 6% (FWHM) at  $E_{max} = 28$  MeV.

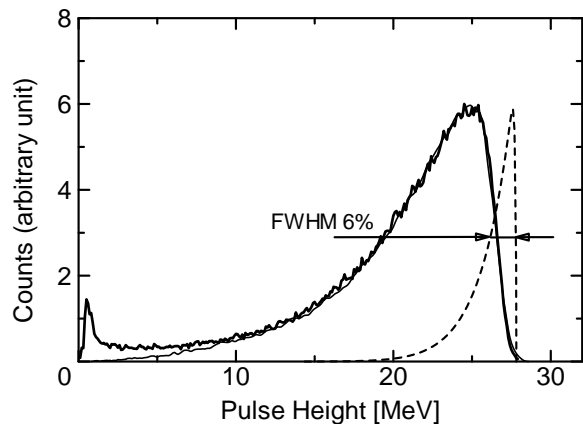


FIG. 19: NaI pulse height spectra obtained for  $E_{max} = 28$  MeV. The thick curve and the thin curve are the measured one and the calculated one, respectively. The dashed curve is an intrinsic energy distribution of the LCS  $\gamma$ -ray required to reproduce the measured spectrum.

#### 5. Photodisintegration of deuteron

The values of  $Y_i$ ,  $\varepsilon_i$ ,  $N_t$ ,  $L$ ,  $\phi$ , and  $\Phi$  were accurately determined as described above, and therefore the photodisintegration cross section of  ${}^4\text{He}$  is determined accurately using the formula of Eq. 1. It is, however, worthwhile to measure the photodisintegration cross section of deuteron to learn about any possible systematic uncertainty of the present experimental method. Note that the cross section has been well studied both experimentally and theoretically in the wide energy range from 10 to 75 MeV [40, 41]. The present measurement was performed using  $\text{CD}_4$  gas instead of  $\text{CH}_4$  gas as the quenching gas of the TPC at  $E_{max} = 22.3$  MeV. The data were analyzed as extensively described above. The cross section turns out to be  $0.56 \pm 0.04(\text{stat}) \pm 0.03(\text{syst})$  mb, which agrees nicely with both the previous data [40] and the theoretical value of 0.55 mb [41] as shown in Fig. 20. The weighted-mean reaction energy was determined as being 21.0 MeV using Eq. 3 and the known energy dependence of the cross section [40, 41]. Hence, the validity of the present experimental method including its analysis was confirmed with a quite small systematic uncertainty within the statistical uncertainty.

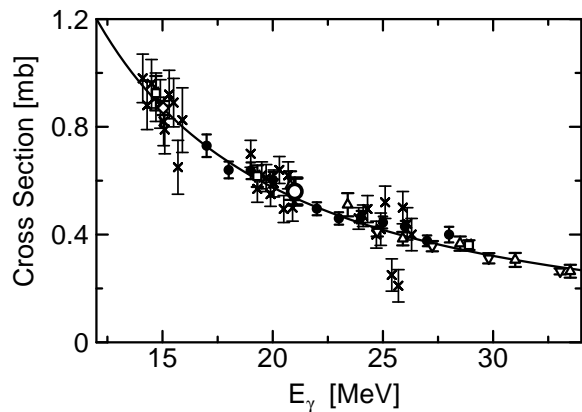


FIG. 20: Cross section of the photodisintegration of deuteron. The open circle denotes the present result, while other symbols indicate the previous data [40]: filled circles; Skopik *et al.*, diagonal crosses; Ahrens *et al.*, open squares; Bernabei *et al.*, open diamonds; Michel *et al.*, open upward triangles; Bosman *et al.*, open downward triangles; Dupont *et al.* The solid curve is the theoretical cross section calculated by means of the momentum-space approach [41].

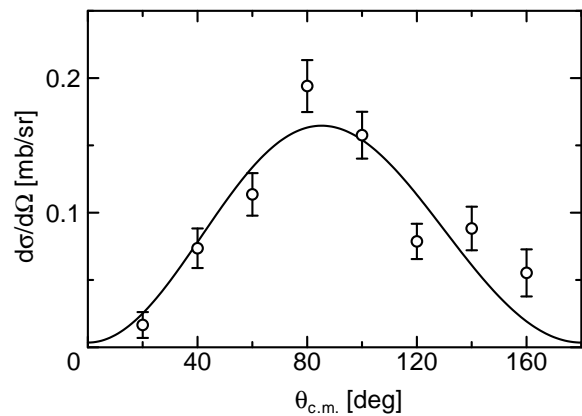


FIG. 21: Differential cross section of the  ${}^4\text{He}(\gamma,p){}^3\text{H}$  reaction at  $\langle E_\gamma \rangle \leq 29.8$  MeV. The open circles denote the measured one in the present work. The solid curve is the fitted one with the least-square method.

#### 6. Angular distribution of proton from the ${}^4\text{He}(\gamma,p){}^3\text{H}$ reaction

In order to determine the electromagnetic property of the photodisintegration at 29.8 MeV we analyzed the angular distribution of charged fragments from the  ${}^4\text{He}(\gamma,p){}^3\text{H}$  reaction at  $E_{max} = 32$  MeV. Note that the two-body total photodisintegration cross section below 26.6 MeV is dominated by E1 radiation as mentioned above [9]. We analyzed data taken at  $E_{max} = 32$  MeV by performing a least-square fit to the data using the following formula [42]:

$$\frac{d\sigma}{d\Omega} = A_0 \cdot (\sin^2\theta_{c.m.} + \beta \cdot \sin^2\theta_{c.m.} \cdot \cos\theta_{c.m.} + \gamma \cdot \sin^2\theta_{c.m.} \cdot \cos^2\theta_{c.m.} + \delta + \epsilon \cdot \cos\theta_{c.m.}). \quad (5)$$

Here,  $\theta_{c.m.}$  is the angle formed by the proton trajectory from the  ${}^4\text{He}(\gamma,p){}^3\text{H}$  reaction with respect to the incident LCS  $\gamma$ -ray beam in the center of mass system.  $A_0$  is determined by the E1 absorption contribution.  $\beta$  is due to the interference of E1 and E2 electric multipoles,  $\gamma$  is the ratio of E2 to E1 absorption probabilities,  $\delta$  is the ratio of M1 to E1 absorption, and  $\epsilon$  is an isotropic term, which is known experimentally to be approximately zero. Consequently, these parameters are determined as  $A_0 = 0.16 \pm 0.02$  mb/sr,  $\beta = 0.17 \pm 0.13$ ,  $\gamma = 0 \pm 0.14$ , and  $\delta = 0.02 \pm 0.01$ . The results indicate the dominance of an electric dipole process in the photodisintegration at

around 30 MeV, and the M1 strength is about 2% of the E1 strength, and the E2 strength is negligible compared to the E1 strength. The present result shown in Fig. 21 is in good agreement with previous data below 26.2 MeV [32] and with a theoretical calculation [9].

#### 7. Cross sections of the two-body and three-body photodisintegration of ${}^4\text{He}$

In order to calculate average cross sections  $\langle \sigma_i \rangle$  of the photodisintegration of  ${}^4\text{He}$  and the weighted-mean

reaction energies  $\langle E_\gamma \rangle_i$  using Eqs. 2 and 3, we first determined the cross sections  $\langle \sigma_i(E_\gamma) \rangle$  using the measured yields of the photodisintegration of  ${}^4\text{He}$  and Eq. 1 as discussed below. Since we made the measurements at four maximum  $\gamma$ -ray energies  $E_{max}$ , we can set up four simultaneous equations as follows:

$$Y_i^{(k)} = N_t \cdot L \cdot \Phi \times \frac{\int_0^{E_{max}^{(k)}} \varepsilon_i(E_\gamma) \cdot \sigma_i(E_\gamma) \cdot \phi^{(k)}(E_\gamma) dE_\gamma}{\int_0^{E_{max}^{(k)}} \phi^{(k)}(E_\gamma) dE_\gamma} \quad (k = 0 \sim 3). \quad (6)$$

Here  $k = 0, 1, 2$  and  $3$  stand for the measurements at  $E_{max} = 22.3, 25, 28$  and  $32$  MeV, respectively.  $Y_i^{(k)}$  is the measured yield of a reaction channel  $i$  of the photodisintegration of  ${}^4\text{He}$  in a measurement  $k$ . Since all the resonance states below  $30$  MeV are known to be quite broad [43], we assume that  $\sigma_i(E_\gamma)$  is a smooth function of  $E_\gamma$  and practically expressed by a power series of the relative momentum  $p$  of the particles in the exit channel as follows:

$$\sigma_i(E_\gamma) = \sum_{j=1}^3 a_j p^j, \quad p = \left( \frac{\mu(E_\gamma - E_i^{th})}{2} \right)^{1/2}. \quad (7)$$

Here  $\mu$  and  $E_i^{th}$  are the reduced mass of the emitted particles and the threshold energy in a reaction channel  $i$ , respectively. The coefficients  $a_j$  were determined by solving Eq. 6 and Eq. 7 simultaneously. Substituting  $\sigma_i(E_\gamma)$  thus obtained for Eqs. 2 and 3, the average cross sections  $\langle \sigma \rangle_i$  and the weighted-mean reaction energies  $\langle E_\gamma \rangle_i$  were obtained. The results for the  $(\gamma, p)$ ,  $(\gamma, n)$ , and total photodisintegration cross sections are given in Table II and shown in Figs. 22(a), 22(b), and 22(c), in which the solid curves represent the most probable functions obtained with the mentioned procedure in the present energy range up to  $32$  MeV. The systematic uncertainties associated with  $\langle \sigma \rangle_i$  were calculated from the uncertainties in  $\varepsilon_i$ ,  $N_t$ ,  $L$  and  $\Phi$ . Due to the similar excitation functions for the  ${}^4\text{He}(\gamma, p){}^3\text{H}$  and  ${}^4\text{He}(\gamma, n){}^3\text{He}$  reactions,  $\langle E_\gamma \rangle$  obtained for both channels agreed with each other within  $100$  keV as expected. Hence, we have used the same values of  $\langle E_\gamma \rangle$  for the  $(\gamma, p)$  and  $(\gamma, n)$  reaction channels.

## IV. DISCUSSION

### A. Ratio of the ${}^4\text{He}(\gamma, p){}^3\text{H}$ cross section to the ${}^4\text{He}(\gamma, n){}^3\text{He}$ cross section

The cross section ratio  $R_\gamma \equiv \sigma(\gamma, p)/\sigma(\gamma, n)$  has been determined accurately with an experimental uncertainty of about  $10\%$  and with small systematic uncertainties in the energy range from  $21.8$  to  $29.8$  MeV. The ratio

is consistent with calculated values without charge symmetry breaking of the strong interaction [1, 8, 46, 47] within the experimental uncertainty as shown in Fig. 23. There, the previous data taken simultaneously for the  ${}^4\text{He}(\gamma, p){}^3\text{H}$  and  ${}^4\text{He}(\gamma, n){}^3\text{He}$  reactions are shown for a comparison. Note that the large ratio, approximately equal to  $2.0$  at  $21.8$  MeV, is due to the difference of the  $Q$ -values between  $n$ - ${}^3\text{He}$  and  $p$ - ${}^3\text{H}$  channels. The ratio at  $26.5$  and  $29.8$  MeV agrees with the latest result obtained by detecting emitted particles from these reactions simultaneously at  $90^\circ$  with respect to the incident beam direction. Our result is also consistent with simultaneous measurements on the  ${}^4\text{He}(e, e'X)$  reaction in the excitation energy region between  $22$  and  $36$  MeV [45] and the  ${}^4\text{He}(p, p'X)$  reaction [44].

### B. The partial and total cross-sections of the photodisintegration of ${}^4\text{He}$

The present  $(\gamma, p)$ ,  $(\gamma, n)$ , and total photodisintegration cross sections of  ${}^4\text{He}$  shown in Figs. 22(a), 22(b), and 22(c) differ significantly from previous data (see below for details).

#### 1. ${}^4\text{He}(\gamma, p){}^3\text{H}$

The  ${}^4\text{He}(\gamma, p){}^3\text{H}$  cross section increases monotonically with energy up to  $29.8$  MeV. The cross section below  $26.5$  MeV does show agreements with none of the previous data while at  $29.8$  MeV it agrees nicely with some of the previous data [12, 25, 27] and marginally agrees with that by Bernabei *et al.* [11]. The value at  $28.6$  MeV in Ref. [11] is in good agreement with an interpolated value of the present data between at  $26.5$  and at  $29.8$  MeV. Note that the present cross section and excitation function significantly differ from the theoretical calculation of the LIT method which predicts a pronounced peak at around  $26$ – $27$  MeV as shown in Fig. 22(a).

#### 2. ${}^4\text{He}(\gamma, n){}^3\text{He}$

The  ${}^4\text{He}(\gamma, n){}^3\text{He}$  cross section shows similar energy dependence as that of the  ${}^4\text{He}(\gamma, p){}^3\text{H}$  as shown in Fig. 22(b), and the value up to  $26$  MeV marginally agree with the data of Berman *et al.* [22] within the experimental uncertainty which includes a systematic error of  $15\%$ . The cross section at  $29.8$  MeV is larger than the previous data [22, 23] by about  $30\%$  but agrees with the data of Gorbunov [25]. The cross section follows the shape of the theoretical calculation based on the AGS method up to  $26$  MeV, although the experimental value is smaller by about  $20\%$  in comparison to the calculation. The experimental result does not agree with the calculation based on the LIT method which predicts a pronounced peak at around  $26$ – $27$  MeV.

TABLE II: Average photodisintegration cross sections of  ${}^4\text{He}$ . The quoted uncertainties are the statistical and systematic ones, respectively.

$\langle E_\gamma \rangle$ [MeV]	$\langle \sigma(\gamma, p) \rangle$ [mb]	$\langle \sigma(\gamma, n) \rangle$ [mb]	$\langle \sigma(\gamma, pn) \rangle$ [mb]	$\langle \sigma_{total} \rangle$ [mb]
21.8	$0.19 \pm 0.02 \pm 0.01$	$0.10 \pm 0.02 \pm 0.006$	—	$0.29 \pm 0.03 \pm 0.02$
24.3	$0.71 \pm 0.05 \pm 0.03$	$0.63 \pm 0.05 \pm 0.03$	—	$1.34 \pm 0.07 \pm 0.06$
26.5	$0.89 \pm 0.06 \pm 0.02$	$0.80 \pm 0.06 \pm 0.02$	—	$1.69 \pm 0.09 \pm 0.04$
29.8	$1.39 \pm 0.08 \pm 0.03$	$1.35 \pm 0.08 \pm 0.03$	$0.04 \pm 0.01 \pm 0.001$	$2.78 \pm 0.11 \pm 0.06$

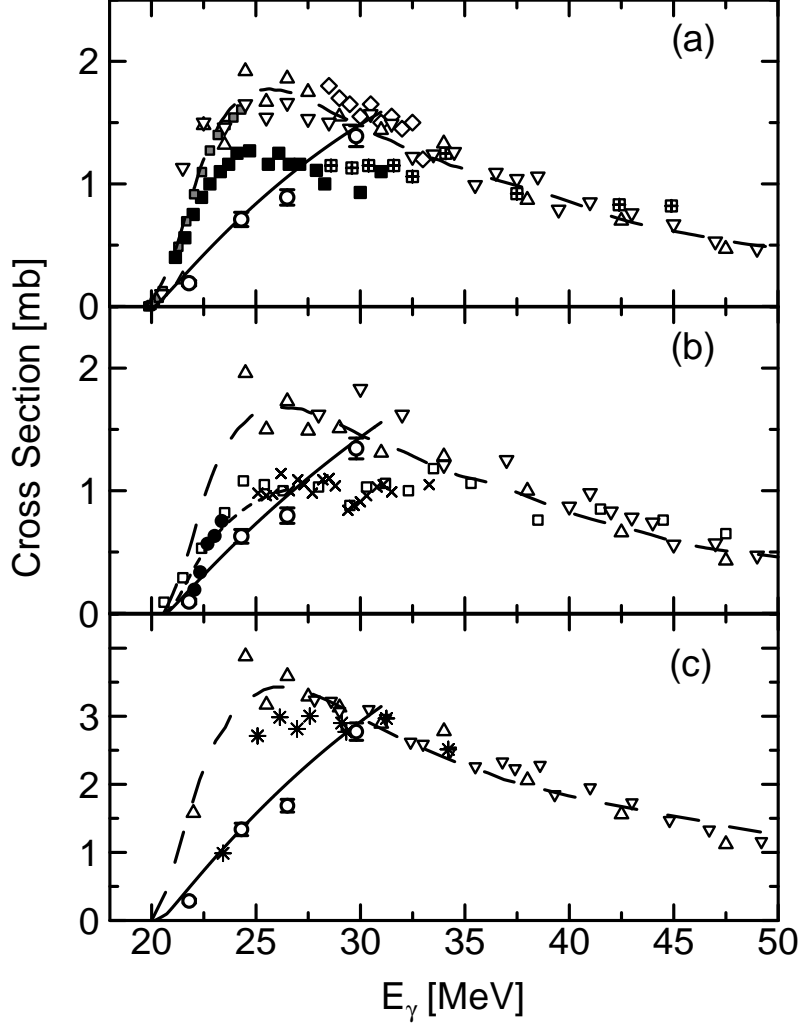


FIG. 22:  ${}^4\text{He}$  photodisintegration cross sections. The solid curves are the most probable functions of the cross sections  $\sigma_i(E_\gamma)$  obtained from the present data in the  $\gamma$ -ray energy range from the reaction threshold up to 32 MeV. The open circles denote the average cross sections  $\langle \sigma \rangle_i$  at the weighted-mean reaction energies  $\langle E_\gamma \rangle_i$ , while other symbols indicate the previous data: (a)  $(\gamma, p)$  cross sections, open upward triangles; Gorbunov [25], open downward triangles; Arkatov *et al.* [27], crossed squares; Bernabei *et al.* [11], filled squares; Feldman *et al.* [18], open diamonds; Hoorebeke *et al.* [12], gray squares; Hahn *et al.* [19], (b)  $(\gamma, n)$  cross sections, open upward triangles; Gorbunov [25], open downward triangles; Arkatov *et al.* [27], open squares; Berman *et al.* [22], diagonal crosses; Ward *et al.* [23], filled circles; Komar *et al.* [24], and (c) total photoabsorption cross sections, open upward triangles; Gorbunov *et al.* [26], open downward triangles; Arkatov *et al.* [27], asterisks; Wells *et al.* [31]. The error bars of the previous data are not shown for clarity. The long-dashed curves are the cross sections calculated using the LIT method with the MTI-III potential [8]. The short-dashed curve represents the calculated  $(\gamma, n)$  cross section based on the AGS formalism [9].

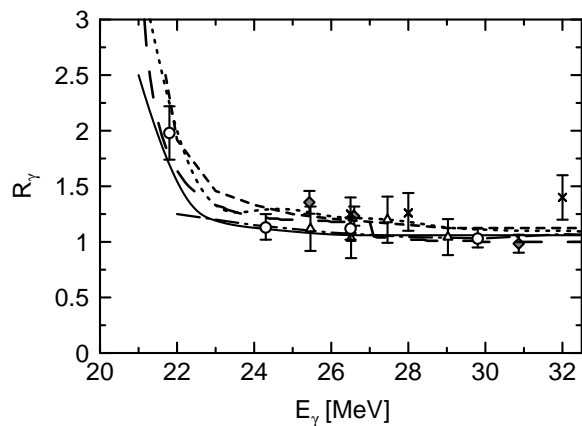


FIG. 23: Ratio  $R_\gamma$  of the  ${}^4\text{He}(\gamma,p){}^3\text{H}$  cross section to the  ${}^4\text{He}(\gamma,n){}^3\text{He}$  cross section: open circles; present result, open triangles; Gorbunov [25], gray diamonds; Balestra *et al.* [29], diagonal crosses; Florizone *et al.* [33]. Short-dashed curve and solid curve are the calculations of the recoil-corrected continuum shell model with and without extra CSB effect, respectively [46]. The long-dashed curve, the dotted curve, and the dash-dotted curve are the calculations without extra CSB based on the LIT method [8], the coupled-channel continuum shell model [47], and the resonating group model [1], respectively.

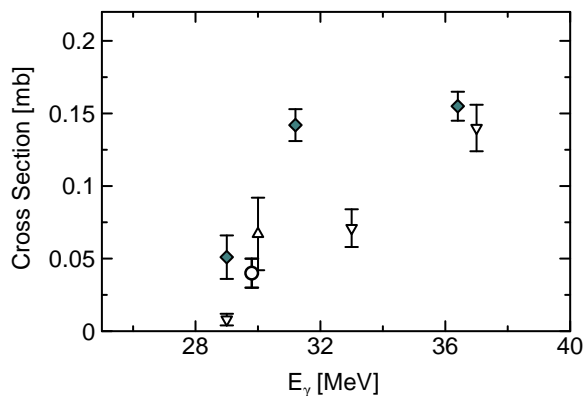


FIG. 24:  ${}^4\text{He}(\gamma,pn){}^2\text{H}$  reaction cross section: open circles; present result, open upward triangles; Gorbunov *et al.* [26], open downward triangles; Arkatov *et al.* [28], gray diamonds; Balestra *et al.* [30].

### 3. ${}^4\text{He}(\gamma,pn){}^2\text{H}$

The small value of the  ${}^4\text{He}(\gamma,pn){}^2\text{H}$  cross section at 29.8 MeV,  $0.04 \pm 0.01$  mb, agrees with previous data as

shown in Fig. 24 [26, 28, 30]. The theoretical calculations on the three-body  ${}^4\text{He}(\gamma,pn){}^2\text{H}$  cross section are not available.

### 4. Total cross section

The total cross section increases monotonically with energy up to 29.8 MeV as shown in Fig. 22(c). The cross section below 26.5 MeV is significantly smaller than previous data [25, 27] and a theoretical calculation based on the LIT method. The cross section at 29.8 MeV agrees with the previous data and with the calculation. Here, it is worthwhile to mention that the total photo-absorption cross-section is inferred from the elastic photon scattering data of  ${}^4\text{He}$  [31] together with previous data of the shape of the photodisintegration cross section, which claim the GDR peak in the region of 25–26 MeV. The cross-section inferred turns out to be  $2.86 \pm 0.12$  mb at around 26 MeV [31], which differs significantly from the present value of  $1.69 \pm 0.09(\text{stat}) \pm 0.04(\text{syst})$  mb at 26.5 MeV. The origin of the discrepancy is not clear, but it could be due to the shape difference between the presently obtained cross section and the previous one. Naturally, it would be interesting to estimate the total photo-absorption cross-section using the shape of the total cross section derived in the present study and the photon scattering cross-section data [31]. Note that the shape can be obtained by combining the present results up to 29.8 MeV with the previous data above around 33–35 MeV, where the previous data agree with each other, as shown in Fig. 22(c).

### 5. E1 sum rule

Since the present cross section is found to be smaller than many previous data and considering that the E1 transition dominates, it is important to investigate the energy distribution of the transition strength. It is well known that the integrated cross section  $\sigma_0$  for E1 photoabsorption and the inverse-energy-weighted sum  $\sigma_B$  can be related to the properties of the ground state of a nucleus through the following sum rules [48, 49]:



$$\sigma_0 = \int_0^{E_\pi} \sigma_{E1}(E_\gamma) dE_\gamma = \sigma_{TRK}(1 + \kappa) = \frac{2\pi^2 e^2 \hbar NZ}{mc A} (1 + \kappa), \quad (8)$$

$$\sigma_B = \int_0^{E_\pi} \frac{\sigma_{E1}(E_\gamma)}{E_\gamma} dE_\gamma = \frac{4\pi^2 e^2 NZ}{3 \hbar c A - 1} \cdot (\langle r_\alpha^2 \rangle - \langle r_p^2 \rangle). \quad (9)$$

Here  $\sigma_{E1}(E_\gamma)$  is the total cross section for E1 photoabsorption as a function of  $E_\gamma$ .  $N$ ,  $Z$ , and  $A$  are the numbers of the neutrons, protons, and nucleons, respectively.  $m$  and  $\kappa$  are the nucleon mass and the correction factor for the contribution of the exchange forces, respectively.  $E_\pi$ ,  $e$ ,  $\hbar$ , and  $c$  stand for the pion threshold energy, electron charge, Planck's constant, and speed of light, respectively.  $\sigma_{TRK}$  stands for the Thomas-Reiche-Kuhn (TRK) sum rule.  $\langle r_\alpha^2 \rangle$  and  $\langle r_p^2 \rangle$  are the mean-square charge radii of  ${}^4\text{He}$  and the proton, respectively. The integrations in Eqs. 8 and 9 have been performed as follows: below 31 MeV we assumed  $\sigma_{E1}(E_\gamma)$  is given as the sum of the present  $\sigma(\gamma, p)$  and  $\sigma(\gamma, n)$ , because the cross section is found to be dominated by the E1 photoabsorption in the two-body channels. Above 31 MeV we employed previous data of Refs. [25, 26] and [27, 54], which are in an overall agreement with each other as well as with recent theoretical calculations. The  $\sigma_0$  and  $\sigma_B$  values are listed in Table III. Here it should be noted that the data taken from Refs. [25, 26] and from Refs. [27, 54] correspond to the cross sections for the total photoabsorption and the E1 photoabsorption, respectively. Therefore the data set of the present result and the cross section from Refs. [25, 26] provides upper limits on  $\sigma_0$  and  $\sigma_B$ . The contributions of higher multipoles have been estimated to be of a few percent [26, 54]. Consequently, the present value of  $\sigma_0$  is marginally lower than the value expected from the other light nuclei [50] and from theoretically predicted values [7, 51]. As for  $\sigma_B$ , the present value is significantly smaller than the calculated value of  $2.62 \pm 0.02$  mb obtained from Eq. 8 using the known experimental values of  $\langle r_\alpha^2 \rangle^{1/2} = 1.673 \pm 0.001$  fm [52] and  $\langle r_p^2 \rangle^{1/2} = 0.870 \pm 0.008$  fm [53].

### 6. Present results and previous data

In the present simultaneous measurement of the  ${}^4\text{He}(\gamma, p){}^3\text{H}$  and  ${}^4\text{He}(\gamma, n){}^3\text{He}$  cross-sections using the  $4\pi$  TPC we could get the cross-section ratio  $R_\gamma = \sigma(\gamma, p)/\sigma(\gamma, n)$  with smaller systematic uncertainties, which is consistent with the results obtained by other reactions as well as with recent simultaneous measurement [33]. However, there are discrepancies between the present two-body and total cross sections and previous ones as described before. Although it is difficult to find a unique reason of the discrepancies since a special care has been taken for the normalization of each of the cross section measured here, it might be instructive to look

at general trends recognized in the previous data and to compare them to the present results.

Firstly we discuss the latest  ${}^4\text{He}(\gamma, p){}^3\text{H}$  data using bremsstrahlung photons [12], which are larger than the data [11] by about 40% at around 30 MeV and are in good agreement with the data [11] at 33 MeV within the experimental uncertainty. Note that the data [11] were obtained using a monochromatic photon beam. This fact may indicate that a possible origin of the above mentioned discrepancy is due to background events inherent to measurement with bremsstrahlung photons. The former group used Si(Li) detectors to detect protons from the  ${}^4\text{He}(\gamma, p){}^3\text{H}$  reaction. They carefully considered possible systematic errors such as the  ${}^4\text{He}$  gas purity, the gas pressure, the efficiency of the Si(Li) detectors, the energy losses in the gas target, the incident flux calibration, the bremsstrahlung shape, the effects due to the background subtraction and others. They had to subtract the background component in the Si(Li) detector assuming an exponential fit to the low-energy photon data. They claimed that the validity of their background subtraction method has been supported by the test measurement of the  ${}^{16}\text{O}(\gamma, p){}^{15}\text{N}$  experiment. However, the cross section of the  ${}^{16}\text{O}(\gamma, p){}^{15}\text{N}$  reaction is about 10 times larger than that of  ${}^4\text{He}$ , and therefore the ambiguity due to the background subtraction might not have been relevant in the test experiment. The contribution of background due to bremsstrahlung photons is expected to decrease with increasing the photon energy, since the energy of an emitted proton becomes higher. Consequently the energy dependence of the difference between the two data sets mentioned above can be explained in this way.

Secondly, we discuss the result of the  ${}^4\text{He}(\gamma, n){}^3\text{He}$  reaction obtained by Berman *et al.* [22], which was carried out using annihilation photon beams and  $\text{BF}_3$  tubes embedded in a paraffin matrix as a neutron counter. They carefully made various corrections due to the background from bremsstrahlung photons, the neutron detector efficiency, and others, and they concluded that their data points at 25.3, 26.3 and 28.3 MeV should have systematic uncertainties as large as 15%. If we take the systematic error in addition to statistical error, our data marginally agree with the data by Berman *et al.* It should be stressed that we used a quasi-monoenergetic pulsed Laser Compton backscattering (LCS) photon beam, which is free from background inherent to bremsstrahlung photon beams, and we detected  ${}^3\text{He}$  unambiguously by the nearly  $4\pi$  TPC containing  ${}^4\text{He}$  gas as an active target. Hence, we could determine the detection efficiency of  ${}^3\text{He}$

TABLE III: Integrated cross section  $\sigma_0$  and inverse-energy-weighted sum rule  $\sigma_B$  for the E1 photoabsorption of  ${}^4\text{He}$ .

$E_\gamma$ [MeV]	Data set	$\sigma_0$ [MeV·mb]	$\sigma_B$ [mb]
19.8–31	Present	$18.1\pm 2.1$	$0.67\pm 0.07$
19.8–135	Present + Refs. [25,52] <sup>a</sup>	$96\pm 7$	$2.24\pm 0.17$
	Present + Refs. [26,53]	$80.4\pm 2.3$	$1.92\pm 0.12$
Sum rule (see text.)		100~128	$2.62\pm 0.02$

<sup>a</sup>Upper limits for E1 contribution.

with high accuracy.

## V. CONCLUSION

In the present work, we have carried out for the first time the direct simultaneous measurement of the two-body and three-body photodisintegration cross sections of  ${}^4\text{He}$  in the energy range from 21.8 to 29.8 MeV using a quasi-monoenergetic pulsed real photon beam by detecting a charged fragment with a nearly  $4\pi$  time projection chamber in an event-by-event mode. The validity of the present new experimental method, including its data analysis, has been accurately confirmed by measuring the photodisintegration cross section of deuteron. By accurately determining the ratio of the  ${}^4\text{He}(\gamma,p){}^3\text{H}$  to  ${}^4\text{He}(\gamma,n){}^3\text{He}$  cross sections, we have solved for the first time the long-standing problem of the large discrepancy in this ratio obtained in separate measurements and simultaneous ones. The  ${}^4\text{He}(\gamma,p){}^3\text{H}$ ,  ${}^4\text{He}(\gamma,n){}^3\text{He}$  and total cross sections do not agree with the recent calculations based on the Lorentz integral transform method. The  ${}^4\text{He}(\gamma,n){}^3\text{He}$  cross section follows the shape of the calculation based on the AGS method up to 26.5 MeV, but it is smaller by about 20% with respect to the calcu-

lated values. We conclude that further theoretical work in the GDR energy region is necessary to elucidate the GDR property of  ${}^4\text{He}$ . Concerning the photonuclear reactions of three-nucleon systems, it has been known that 3NF reduces the peak cross section by about 10–20% [56]. Since  ${}^4\text{He}$  is tightly bounded compared to the three-nucleon systems, one might expect significant 3NF effects in the photodisintegration of  ${}^4\text{He}$ . The present result would affect significantly the production yields of r-nuclei by the neutrino-induced r-process nucleosynthesis, since the neutral current neutrino spallation cross sections are quite sensitive to the peak energy of the GDR and the cross section in the GDR energy region.

## Acknowledgments

We would like to thank Profs. H. Kamada and T. Kajino for discussions, and Dr. A. Mengoni for comments and careful reading of the manuscript. The present work was supported in part by Grant-in-Aid for Specially Promoted Research of the Japan Ministry of Education, Science, Sports and Culture and in part by Grant-in-Aid for Scientific Research of the Japan Society for the Promotion of Science (JSPS).

- 
- [1] M. Unkelbach and H. M. Hofmann, Nucl. Phys. A549, 550 (1992).
- [2] F. C. Barker and A. K. Mann, Philos. Mag. 2, 5 (1957).
- [3] S. E. Woosley, D. H. Hartmann, R. D. Hoffman, and W. C. Haxton, Ap.J. 356, 272 (1990).
- [4] B. S. Meyer, Ap.J. 449, L55 (1995).
- [5] S. A. Sofianos, H. Fiedeldey, and W. Sandhas, Phys. Rev. C48, 2285 (1993).
- [6] B. Wachter, T. Mertelmeier, and H. M. Hofmann, Phys. Rev. C38, 1139 (1988), and references therein.
- [7] V. D. Efros, W. Leidemann, and G. Orlandini, Phys. Rev. Lett. 78, 4015 (1997); N. Barnea, V. D. Efros, W. Leidemann, and G. Orlandini, Phys. Rev. C63, 057002 (2001).
- [8] S. Quaglioni, W. Leidemann, G. Orlandini, N. Barnea, and V. D. Efros, Phys. Rev. C69, 044002 (2004).
- [9] G. Ellerkmann, W. Sandhas, S. A. Sofianos, and H. Fiedeldey, Phys. Rev. C53, 2638 (1996); W. Sandhas, W. Schadow, G. Ellerkmann, L. L. Howell, and S. A. Sofianos, Nucl. Phys. A631, 210c (1998).
- [10] J. Golak, R. Skibiński, W. Glöckle, H. Kamada, A. Nogga, H. Witała, V. D. Efros, W. Leidemann, G. Orlandini and E. L. Tomusiak, Nucl. Phys. A707, 365 (2002).
- [11] R. Bernabei *et al.*, Phys. Rev. C38, 1990 (1988).
- [12] L. Van Hoorebeke, R. Van de Vyver, V. Fiermans, D. Ryckbosch, C. Van den Abeele, and J. Dias, Phys. Rev. C48, 2510 (1993).
- [13] C. C. Gardner and J. D. Anderson, Phys. Rev. 15, 626 (1962).
- [14] D. S. Gemmell and G. A. Jones, Nucl. Phys. 33, 102 (1962).
- [15] W. E. Meyerhof, M. Suffert, and W. Feldman, Nucl. Phys. A148, 211 (1970).
- [16] R. C. McBroom, H. R. Weller, N. R. Roberson, and D. R. Tilley, Phys. Rev. C25, 1644 (1982).
- [17] J. R. Calarco, S. S. Hanna, C. C. Chang, E. M. Diener, E. Kuhlmann, and G. A. Fisher, Phys. Rev. C28, 483 (1983).
- [18] G. Feldman, M. J. Balbes, L. H. Kramer, J.Z. Williams, H. R. Weller, and D. R. Tilley, Phys. Rev. C42, R1167 (1990).
- [19] K. I. Hahn, C. R. Brune, and R. W. Kavanagh, Phys.

- Rev. C51, 1624 (1995).
- [20] J. D. Irish, R. G. Johnson, B. L. Berman, B. J. Thomas, K. G. McNeill, and J. W. Jury, Phys. Rev. C8, 1211 (1973).
- [21] C. K. Malcom, D. V. Webb, Y. M. Shin, and D. M. Skopik, Phys. Lett. B47, 433 (1973).
- [22] B. L. Berman, D. D. Faul, P. Meyer, and D. L. Olson, Phys. Rev. C22, 2273 (1980).
- [23] L. Ward, D. R. Tilley, D. M. Skopik, N. R. Roberson, and H. R. Weller, Phys. Rev. C24, R317 (1981).
- [24] R. J. Komar, H.-B. Mak, J. R. Leslie, H. C. Evans, E. Bonvin, E. D. Earle, and T. K. Alexander, Phys. Rev. C48, 2375 (1993).
- [25] A. N. Gorbunov, Phys. Lett. B27, 436 (1968).
- [26] A. N. Gorbunov and V. M. Spiridonov, Zh. Eksp. Teor. Fiz. 34, 866 (1958) [Sov. Phys. JETP, 7, 600 (1958)].
- [27] Yu. M. Arkatov, P. I. Vatsset, V. I. Voloshchuk, V. A. Zolenko, I. M. Prokhorets, and V. I. Chmil', Yad. Fiz. 19, 1172 (1974) [Sov. J. Nucl. Phys. 19, 598 (1974)].
- [28] Yu. M. Arkatov, A. V. Bazaeva, P. I. Vatsset, P. I. Voloshchuk, A. P. Klyucharev, and A. F. Khodyachikh, Yad. Fiz. 10, 1123 (1969) [Sov. J. Nucl. Phys. 10, 639 (1970)].
- [29] F. Balestra, E. Bollini, L. Busso, R. Garfagnini, C. Guaraldo, G. Piragino, R. Scrimaglio, and A. Zanini, Nuovo Cim. 38A, 145 (1977).
- [30] F. Balestra, L. Busso, R. Garfagnini, G. Piragino, and A. Zanini, Nuovo Cim. 49A, 575 (1979).
- [31] D. P. Wells, D. S. Dale, R. A. Eisenstein, F. J. Federspiel, M. A. Lucas, K. E. Mellendorf, A. M. Nathan, and A. E. O'Neill, Phys. Rev. C46, 449 (1992).
- [32] D. J. Wagenaar, N. R. Roberson, H. R. Weller and D. R. Tilley, Phys. Rev. C39, 352 (1989).
- [33] R. E. J. Florizone, J. Asai, G. Feldman, E. L. Hallin, D. M. Skopik, J. M. Vogt, R. C. Haight, and S. M. Sterbenz, Phys. Rev. Lett. 72, 3476 (1994).
- [34] H. Ohgaki, S. Sugiyama, T. Yamazaki, T. Mikado, M. Chiwaki, K. Yamada, R. Suzuki, T. Noguchi, and T. Tomimasu, IEEE Trans. Nucl. Sci. 38, 386 (1991).
- [35] T. Kii, T. Shima, T. Baba and Y. Nagai, Nucl. Instr. Meth. A, in press.
- [36] H. H. Andersen and J. F. Ziegler, *Hydrogen Stopping Powers and Ranges in All Elements*, vol. 3 of series *Stopping and Ranges of Ions in Matter*, Pergamon Press, New York (1977); J. F. Ziegler, *Helium Stopping Powers and Ranges in All Elements*, vol. 4 of series *Stopping and Ranges of Ions in Matter*, Pergamon Press, New York (1978); U. Littmark and J. F. Ziegler, *Handbook of Range Distributions for Energetic Ions in All Elements*, vol. 6 of series *Stopping and Ranges of Ions in Matter*, Pergamon Press, New York (1980).
- [37] H. R. Weller and D. Lehman, Annu. Rev. Nucl. Part. Sci. 38, 563 (1988); G. Blüge, H. J. Assenbaum, and K. Langanke, Phys. Rev. C36, 21 (1987); H. J. Assenbaum and K. Langanke, Phys. Rev. C36, 17 (1987); B. Wachter, T. Mertelmeier and H. M. Hofmann, Phys. Lett. B200, 246 (1988).
- [38] H. Toyokawa, T. Kii, H. Ohgaki, T. Shima, T. Baba and Y. Nagai, IEEE Trans. Nucl. Sci. 47, 1954 (2000).
- [39] S. Agostinelli *et al.*, Nucl. Instr. Meth. A 506, 250 (2003).
- [40] R. Bernabei *et al.*, Phys. Rev. Lett. 57, 1542 (1986), and references therein; C. Dupont, P. Leleux, P. Lipnik, P. Macq and A. Ninane, Nucl. Phys. A445, 13 (1985); P. Michel, K. Moller, J. Mosner and G. Schmidt, J. Phys. G. 15, 1025 (1989).
- [41] H. Arenhövel and M. Sanzone, *Photodisintegration of the Deuteron (Few-Body Systems Suppl. 3)*, Springer-Verlag, Wien, 1991.
- [42] E. A. Vinokurov *et al.*, Yad. Fiz. 49, 1233 (1989) [Sov. J. Nucl. Phys. 49, 767 (1989)]; R.T. Jones, D. A. Jenkins, P. T. Debevec, P. D. Harty, and J. E. Knott, Phys. Rev. C 43, 2052 (1991).
- [43] D. R. Tilley, H. R. Weller and G. M. Hale, Nucl. Phys. A541, 1 (1992).
- [44] B. A. Raue *et al.*, Phys. Rev. C52, R445 (1995).
- [45] M. Spahn, Th. Kihm, K. T. Knöpfle, J. Friedrich, N. Voegler, Ch. Schmitt, V. H. Walther, M. Unkelbach, and H. M. Hofmann, Phys. Rev. Lett. 63, 1574 (1989).
- [46] D. Halderson and R. J. Philpott, Phys. Rev. C28, 1000 (1983).
- [47] J. T. Londergan and C. M. Shakin, Phys. Rev. Lett. 28, 1729 (1972).
- [48] J. S. Levinger and H. A. Bethe, Phys. Rev. 78, 115 (1950); M. L. Rustgi and J. S. Levinger, Phys. Rev. 106, 530 (1957).
- [49] L. L. Foldy, Phys. Rev. 107, 1303 (1957).
- [50] J. Ahrens *et al.*, Nucl. Phys. A251, 479 (1975).
- [51] W. Heinze, H. Arenhövel and G. Horlacher, Phys. Lett. B76, 379 (1978); M. Gari, H. Hebach, B. Sommer and J. G. Zabolitzky, Phys. Rev. Lett. 41, 1288 (1978).
- [52] E. Borie and G. A. Rinker, Phys. Rev. A18, 324 (1978).
- [53] Particle Data Group, Phys. Lett. B592, 67 (2004).
- [54] Yu. M. Arkatov, P. I. Vatsset, V. I. Voloshchuk, V. A. Zolenko, and I. M. Prokhorets, Yad. Fiz. 31, 1400 (1980) [Sov. J. Nucl. Phys. 31, 726 (1980)].
- [55] A. Arima, G. E. Brown, H. Hyuga and M. Ichimura, Nucl. Phys. A205, 27 (1973).
- [56] R. Skibiński, J. Golak, H. Kamada, H. Witała, W. Glöckle, and A. Nogga, Phys. Rev. C67, 054001 (2003).